Simultaneous Eulerian-Lagrangian velocity measurements of particulate pipe flow in transitional regime

Singh, S., Potherat, A., Pringle, C., Bates, I. & Holdsworth, M.

Original citation & hyperlink:
Singh, S, Potherat, A, Pringle, C, Bates, I & Holdsworth, M 2020, 'Simultaneous Eulerian-Lagrangian velocity measurements of particulate pipe flow in transitional regime', Review of Scientific Instruments, vol. 91, no. 9, 095110.
https://dx.doi.org/10.1063/1.5129062

DOI 10.1063/1.5129062
ISSN 0034-6748
ESSN 1089-7623

Publisher: American Institute of Physics

Simultaneous Eulerian-Lagrangian velocity measurements of particulate pipe flow in transitional regime

S. Singh,* A. Pothérat, C. C. T. Pringle, I. R. J. Bates, and Martin Holdsworth
Fluid and Complex Systems Centre, Coventry University, Coventry, CV1 5FB, UK.
(Dated: August 26, 2020)

We present a unique pipe flow rig capable of simultaneous particle tracking and flow velocity measurements in a dilute, neutrally buoyant particulate pipe flow in regimes of transition to turbulence. The flow consists of solid glass spheres for the disperse phase, and a density-matching fluid for the carrier phase. The measurements are conducted using a bespoke, combined two-dimensional Particle Image Velocimetry (PIV) and Particle Tracking Velocimetry (PTV) technique. The technique takes advantage of a phase discrimination approach that involves separating the disperse and carrier phases based on their respective image characteristics. Our results show that the rig and the technique it implements can effectively be employed to study transitional particulate pipe flows at dilute concentration.

I. INTRODUCTION

Adding particles, even in moderate amounts to an otherwise Newtonian flow can drastically alter its global properties. For instance, they are commonly added into pipes to reduce drag in various industrial applications [1, 2]. While in some cases, particulate flows seem to transition to turbulence at higher Reynolds numbers than their single phase counterpart, the underlying mechanisms are not understood. One of the reasons is the lack of experiments targeting the transitional regimes, where both fluid and particles can be tracked simultaneously and separately. The purpose of this work is precisely to address this gap, in the canonical case of particulate pipe flows and neutrally buoyant particles.

Transition in particulate pipe flow is much more complex than in single phase flow in that it is not only determined by the flow rate but also the particles size and concentration. Despite wide applications in industries such as oil and gas or chemical and food processing, it has not been studied extensively. Early experiments on the transition to turbulence in a pipe highlighted a critical volume fraction of particles below which they favoured the transition at a lower Reynolds number. At higher volume fractions, by contrast, this effect was reversed [3]. Recent numerical simulations based on accurate modelling of individual solid particles recovered this phenomenology for pipe [4] and channel flows [5]. Between very small particles that passively trace the flow and large ones which ignore it, there is an intermediate optimal size of particles which have the greatest effect on the flow. Here, adding only minimal additional physics is sufficient to greatly alter the linear growth of modal and non-modal perturbations [6–9] to the point of making pipe flows linearly unstable [10].

Several experiments [11–13] have provided a more quantitative description of the dynamics of transition in single phase pipe flow, and its flow structures during the transitional phase [14–16]. A more detailed review of some of the experiments in pipe flows can be found here [17]. The main feature of the pipe flow problem is the sub-critical nature of its transition to turbulence that makes it highly sensitive to external disturbances. As far as experiments are concerned, extreme care is needed to keep out unwanted perturbations and introduce only controlled ones, so as to precisely identify the conditions of the transition. In regards to experiments in particulate pipe flow, [3] quantified transition by pressure drop measurements, [18, 19] looked at the effects of volume fractions on transition scenarios and identified regimes where transition scenarios were different from that in a single Newtonian fluid. While [18] measured the fluid velocity only using Ultra sound image velocimetry (UIV), simultaneous measurement of fluid-particle remains elusive for neutrally buoyant, particulate pipe flow in the transitional regimes. These experiments have increased our understanding of transition in particle-laden flow, however, the role played by particles in instigating transition is still not clear. The measurement systems used in these experiments are "blind" to particles and effective only at diagnosing the particles' effect on the carrier phase. In regards to the universality of the transition regimes [18, 19], further experimental data is needed, varying particle sizes and different perturbation systems to consider this question closed. Additionally, the regimes considered by [10] that are suggestive of possible instability have also not been explored.

Measuring the velocities of both the fluid and the particles by optical means require two distinct techniques. Using Particle Image Velocimetry (PIV), the instantaneous whole field velocity (Eulerian) of single phase can be measured. In particle-laden flow, by contrast, a low image density technique such as Particle Tracking Velocimetry (PTV) typically provides the Lagrangian velocity of the disperse phase velocity. However, these techniques become quite challenging when implemented simultaneously, and successful implementation would require a trade-off. A moderate concentration of discrete particles leads to an overload of optical signal from the solid particles in the images. This incurs restrictions on the concentration of discrete particles [20]. Furthermore, the difficulty in distinguishing the signals from each phase often causes false positive cross correlation between them, also known as "cross-talk" [21, 22].

To circumvent this issue, a phase discrimination method based on image intensity is implemented to separate the phases by dynamic masking. In this method, image thresholding and image feature selection are used to identify the disperse phase which subsequently generates the disperse phase velocities.

* sanjaysingh88@gmail.com

For the fluid phase velocity, the identified disperse phase undergoes dynamic masking before the PIV processing techniques. The details of this method are elaborated further in Sect. III C. The main challenge in this approach is to accurately discriminate between the dispersed phase and the carrier phase. In the past, this has been tackled in several ways: [21] used fluorescent particle tagging to optically separate the signal between the fluorescent tracer and particles; [23–25] and [26] separated the phases by image processing based on the relative sizes and optical scattering of the tracers and particles; [27] expanded on previous work of [28] by implementing versatile image filters and particle size-brightness maps; [29] used combination of both the methods to study turbulent particle-laden flow. In other notable research works, phase separation was achieved by ensemble correlation algorithm [30], by edge detection of bright features [22], whereas [31] used erosion and dilation techniques to separate the phases before processing the PIV and PTV using the Digiflow software [32]. Furthermore, generating individual logical masks (dynamic masking) over each frames pose difficulties when the particles and tracers have small contrast, and if the uneven illumination causing inhomogeneous background cannot be removed with background subtraction [22]. Such issues can be mitigated by evenly illuminating the plane with a thin light sheet and using a shallow depth of field. Logical masks obtained by padding zeros to the particle features can create "coronas" from the edges of particles that were not masked properly, resulting in erroneous cross-correlation. This issue can be mitigated by pre-processing the masked images with a median filter [22]. Failing that, one can resort to recent advanced techniques [33, 34]. However, if the particle shape is known *a priori*, masks of same sizes as that of particle detected can be implemented without implementing computationally costly algorithm. One of the inherent limitations of PIV techniques is that at high particles volume fraction ($> 10^{-3}$), obscuration prevents optical measurements. This can be overcome by carefully matching the refractive indices of the solid and the carrier phases [35], and implementing Refractive Index Matching (RIM) PIV [36]. However, there are limitations posed by the PTV tracking algorithm which cannot identify particles correctly anymore [20]. Additionally, with more solid particles detected and masked, higher regions of missing vectors in the fluid phase cause significant data loss [30], the interpolation of which results in spurious nonphysical results [21].

While there are several particle tracking methods [37–39], each of them have their own strengths and limitations in terms of particle tracking capabilities, implementation and computational costs. A common strategy found in tracking algorithms is to look for the nearest neighbour in a search window [40], however the data yield in such algorithm is poor since it ends particle tracks in the event of an overlap between particles. Multi-frame tracking [41, 42] performs well in such situations by starting new tracks. However, tracking still remains challenging in 2D PIV where tracks are inherently short because particles move in and out of a thin LASER sheet. A 3D PTV system such as the one used in turbulent pipe flow measurements by [43], or one with advanced tracking features based on neural network techniques [44] would be able to reconstruct short, broken tracks; however, it would still suffer from data loss due to masking. Furthermore, there are no measurement systems yet that can simultaneously perform full Lagrangian tracking of particles and solids. This capability is currently only available in numerical simulations [45].

The vast majority of research work in this area shows clearly how complex these techniques are, and that there are no generic solutions that would fit and reconcile all experimental difficulties. Alternatives to PIV techniques to diagnose high volume fraction "opaque" flows exits: magnetic resonance imaging (MRI), however, it only provides Eulerian fluid velocities [46]; a similar limitation is seen in ultrasound imaging velocimetry (UIV) [18, 47]. Techniques such as positron emission particle tracking (PEPT) are capable of providing velocity information of radioactive tracers (single phase) in Eulerian and Lagrangian frames [48], but have low spatial resolution compared to PIV systems. To the best of our knowledge, simultaneous solid-liquid velocity measurements for the transitional regime in particle laden flow are not available. Experiments of this nature with non-linear response to finite perturbations require a carefully controlled rig design with minimal experimental and ambient perturbation. Here we present a rig that has been specifically built to satisfy both sets of constraints. Whilst it elaborates on a number of techniques previously used in other rigs, the technical challenge resides in combining them into a single device.

In this context, we focus on Eulerian and Lagrangian velocity measurements conducted in a neutrally buoyant, particulate flow in a circular, horizontal pipe where both the experimental constraints imposed by transitional flows and those of two-phase velocity mapping are met. The measurements are obtained by separating the dispersed and carrier phases using image brightness, and applying a combined 2D particle image/tracking velocimetry (PIV/PTV) technique to map the flow fields. The paper begins with a description of the two-phase facility, highlighting the design elements adopted from previous experiments for a precise control of experimental parameters (Section II); followed by presentation of the PIV/PTV measurement technique, including the steps involved in image processing and calibration to obtain the velocity fields (Section III). Finally, velocity measurements for both the solid and fluid phases are presented in Sect. IV.

II. THE TWO PHASE PIPE FACILITY

A. Description

The rig consists of an assembly of glass pipes through which fluid and particles flow at a constant mass flux as shown in Fig.1. The reason for this choice is two-fold: First, this arrangement is capable of setting the flow velocity in a more controlled manner compared to pressure-driven systems [11]. Second, it avoids the sort of pressure fluctuations that prevents the accurate setting of flow rate [3]. This point is crucial as we are interested in transitional flows, which are likely to be sensitive to finite amplitude perturbations. This constraint

imposes a very controlled, and precise design such that the disturbances introduced from the experimental rig are kept to a minimum. For these reasons, the rig functions as an open loop: the pipe is fed by a header tank and both fluid and particles are pulled through it by a piston whose motion is controlled by a linear motor. We shall describe the details of its design, manufacture and performance. The key features of the facility are listed in Table I.

a. Pipe section and its assembly. The glass pipe has been assembled in 10 sections of cylindrical borosilicate glass tubes (GPE Scientific Ltd.). Each section is 1.2 m ($\pm$0.01 mm) long with an inner bore diameter $D = 20 \pm 0.01$ mm, and a wall thickness of 3.1 $\pm$0.03 mm. This configuration provides a ratio of the effective length of the pipe L to diameter D, $L/D = 615$. Prior to their assembly, variation in concentricity of the pipe diameters were measured within a range of $\pm$10-30 μm by means of a 3-axis coordinate measuring machine, by mapping the maxima and minima of the inner and outer diameters of each pipe sections. This was taken as a tolerance limit for the manufacture of machined-to-fit Aluminium male/female flanges that served as unions between the pipe sections. The flanges were attached by pouring epoxy rubber to the pipe ends after carefully positioning them in a vertical jig on a rigid table. The jig consisted of a mandrel which ensured that both the pipe end, and the flanges were concentric, whereas the pourable rubber served to compensate for any expansion/contraction arising from temperature variations. The flange design and the assembly method were inspired from the Very Large Scale Pipe Flow (VLSPF) facility at the University of Liverpool [49].

Using selective assembly, these pipe sections with unions attached were joined in a tight fit ranging from 10-30 μm. Male and female unions are separated by a rubber O-ring and PTFE tape to prevent any potential leak. To maintain the overall end-to-end straightness and horizontality of the pipe assembly, a target tool and a self-levelling LASER (Bosch) were used. The precision of the assembly is such that the LASER fired at one end of the long pipe assembly hits a target dot of 3 mm diameter within $\pm$ 0.5 mm at the other end. The entire assembly rests on Aluminium profiles, with each union held by rubber-reinforced clamps supported on adjustable threaded screws. This arrangement ensures that the overall horizontality of the entire rig is not affected by any slope in the floor, in addition to providing an isolation from vibrations emanating from the ground. Moreover, a gutter system is in place all along the rig to contain any potential spillage of the working fluid. The pipe is fed by a rectangular header tank made of perspex with an inner volume of 62 l. A custom-made bell-mouth shaped inlet is attached to a shorter pipe section of 0.30 m in length. This inlet is placed at the centre of the header tank (0.25 m$\times$0.25 m$\times$1 m) so as to minimise perturbations from the inlet walls, and joined to the rest of pipe sections through a flange on the tank wall.

b. Working fluid and solid/liquid phases. The liquid and solid phases are critical elements of the rig that must satisfy combined optical and mechanical constraints: First, the liquid must be transparent to allow for optical measurement techniques and the particles must be sufficiently reflective not only to be detectable, but also distinguishable from the tracers used to measure the fluid velocity measurements.
Second, fluid and particles must have matched density to cancel any buoyancy force. To satisfy both conditions, we chose an aqueous solution of Sodium Polytungstate (TC-Tungsten Compounds GmbH), obtained by diluting crystals in deionised water. The main advantage of this choice is that the fluid's density can be adjusted to match the density of the solid phase with an accuracy of 1 kg/m^3, simply by changing the dilution.

For the purpose of our experiment, the solution has the following properties: density, ρ_f= 2500 Kg/m^3; dynamic viscosity, η = 11-14 $\pm$0.001 mPa.s (at room temperature, T_r= 17°-21°C), and refractive index, n= 1.524 $\pm$0.0001 (measured with a Kern Optics digital refractometer). These quantities are measured experimentally prior to each set of measurements. The density (Densitometer, Anton Parr) and the viscosity (Viscolite 700, Hydramotion) readings are temperature-compensated measurements. The fluid is Newtonian with sufficient optical transparency for PIV techniques.

However, the fluid undergoes a reduction reaction when in contact with any base metals (exception: Stainless steel, and some grades of Aluminium), resulting in a discolouration which prevents optical measurements. To avoid this issue, extreme care has been taken in choosing the materials in such a way that the fluid only comes in direct contact with glass, perspex, rubber material and anodised Aluminium parts.

The density of the fluid has been adjusted to match that of standard spherical, monodisperse glass beads used for the solid phase (density ρ_s= 2500 Kg/m^3, n= 1.50, Boud Minerals Ltd.), to achieve neutral buoyancy. The glass beads are graded using ISO standard sieves into required sizes (diameter, d_p =150 μm $\pm$10 μm) and introduced in the fluid at a controlled volume fraction C of 10^{-5} or more. This simple methodology makes available to us monodisperse particles with a precisely controlled diameter in large enough quantities to fill the entire volume of the rig (62 l), at a reasonable cost. Furthermore, the close match between the refractive index of the fluid and glass beads could potentially allow measurements at higher volume fraction otherwise inaccessible to typical PIV measurements [35].

Finally, for the purpose of optical measurements, the liquid is also seeded with smaller sized (d_t= 32-38 μm), silver-coated hollow glass microspheres (Cospheric) of nearly the same density, ρ_t= 2580 kg/m^3 as the working fluid. These act as tracers passively following the fluid phase. The low settling velocity and low stokes number of the tracers ($St_{tracer} = 3.088 \times 10^{-4}$) ensures that they remain in suspension for hours and passively follow the fluid's motion.

c. Constant mass flux system. To ensure a constant mass flux, the fluid is drawn in by a system that consists of a modified pneumatic cylinder (Camozzi), 1 m in length and 0.20 m in inner diameter. The stainless steel piston of this cylinder is driven by an actuation system that is made of a lead screw (IGUS, stroke length: 1.250 m, pitch: 5 mm), coupled to a DC motor (Oriental Motor, 200 W, Max. rated speed: 3000 RPM, Gear ratio: 20) with a dedicated speed controller (Oriental Motor, BLE2 series). The actuation system precisely sets the

TABLE I: Summary of the physical features of the rig.

Pipe	Diameter, D	20 mm
	Length, L	12.3 m
	Material	Borosilicate glass
	Wall thickness	3.1 mm
Flow	Fluid phase	Sodium Polytungstate
	Fluid density, ρ_f	2500 Kg/m^3
	Solid phase	Solid Glass beads
	Glass bead density, ρ_s	2500 Kg/m^3
Seeding	Type	Silver-coated hollow glass spheres
	Density, ρ_t	2540 Kg/m^3
	Diameter, d_t	32-38 μm

flowrate (the precision of ± 1 mm/s on piston speed translates into $\pm$ 1.88 l/min for the flowrate), which is also independently monitored by means of an Electromagnetic flowmeter (OMEGA, 5 to 250 l/min $\pm$ (1.5% of reading + 0.3% of range)). In addition, the rotation of the lead screw is monitored using an encoder to ensure that the variations in linear velocity are well below 1%.

d. Perturbation system. To study the effects of finite amplitude perturbations on the stability of the flow, a perturbation generator has been devised that injects a small volume of fluid ($\sim$0.1% of total mass flow) to the base flow [12, 50]. The system consists of an inlet (30 mm long, borosilicate glass inlet tube of inner bore of 2.2 mm) seamlessly attached to the top mid-section of one of the pipe sections. The perturbation is a radial jet of fluid which is injected by a syringe coupled to a lead screw, itself driven by a stepper motor. The fluid volume to be injected is extracted from the pipe during the syringe's retraction, and replenished in-between experimental runs. This is to ensure that the particle and tracer concentration remain constant. The jet is introduced at a distance of $225D$ downstream from the inlet. In all experiments, the flow is well established at that point. Alternative strategies to introduce perturbations in the flow and their respective merits are reviewed in [17].

B. Control parameters

The flow is determined by three non-dimensional control parameters: Classical pipe flows are solely controlled by the Reynolds number $Re = \mathscr{U} D/\nu$, which represents the ratio of inertia to viscous forces at the pipe scale in the fluid phase. Here, $\mathscr{U} = \frac{8}{D^2}\langle \int_0^r u_x(r) r dr \rangle_t$ is the average velocity of the fluid in the pipe of radius r, u_x is the streamwise velocity and $\nu = \eta/\rho_f$ is the kinematic viscosity. $\langle . \rangle_t$ denotes a time average. Since the added particles are spherical, they are parametrised by their radius and concentration, which adds two independent control parameters: the Stokes number, $St = \tau_p/\tau_t$, classically measures the ratio of the particle's relaxation time under the effect of drag, $\tau_p = \rho_p {d_p}^2/18\eta$, and

Re	800-5060	0.21-1.33	$\mathscr{U}$ (m/s)
St	0.001-0.01	150-500	d_p (μm)
C	10^{-6}-10^{-3}		

TABLE II: Range of Physical and non-dimensional control parameters currently accessible in the rig.

fluid's advection time $\tau_t = D/\mathscr{U}$. It is worth noting that the Stokes number St is not an effective measure of the particle response time to the fluid time scale in a neutrally-buoyant case where there is no large density difference. In such cases, the Stokes drag is not the dominant contributor to controlling the particle motion. However, while St is small for the 150 μm particles, it may become sufficiently large and thus represent dominant drag forces, in future experiments with larger particle size (typically 500 μm). For particles of diameter 150 μm, the terminal settling velocity was found to be $v_s \simeq 0.943$ μm/s with a settling timescale of $\tau_s = D/v_s \simeq 6$ hours. Due to the matching densities of the solid particles and the fluid, the particles should in principle remain in suspension as they are neutrally buoyant. However, in reality, density of the dispersed phase varies from particle to particle such that eventually some of the particles rise, while others sink under the mean matched conditions. Lastly, the ratio of the total particle volume in the pipe to the working volume of the fluid yields the volume fraction of the particles C. These parameters are independently controlled in the experiment, by controlling the total flowrate (Re), particle diameter (St) and the amount of particles seeded in the flow (C). The range of accessible Reynolds numbers is determined by the minimum and maximum velocity of the piston and the maximum acquisition frequency of the optical system. In theory, the Stokes number can be adjusted to any value between micro-metric particles to spheres as large as the pipe allows. The concentration, on the other hand is limited by the reduction in optical visibility that occurs at high concentrations. This effect can be mitigated by the near-identical refractive indices of the fluid and the glass beads. However, our combined PIV-PTV system does not operate at concentrations greater than 0.1%. A summary of the range of physical and non-dimensional parameters is provided in Table II.

III. MEASUREMENT SYSTEM: PIV/PTV

A. Optical system

As discussed in the introduction (see Sect.I), simultaneous measurement of fluid/solid velocities in particle-laden flow is challenging due to presence of two sources of optical signals: tracers (used for the measurement of fluid velocity) and particles made of glass beads. Accurately separating the phases and measuring their respective velocities require a specific design of the optical measurement system. Consequently, a bespoke system has been devised to map the Eulerian and Lagrangian velocities of the carrier fluid and the solid particles.

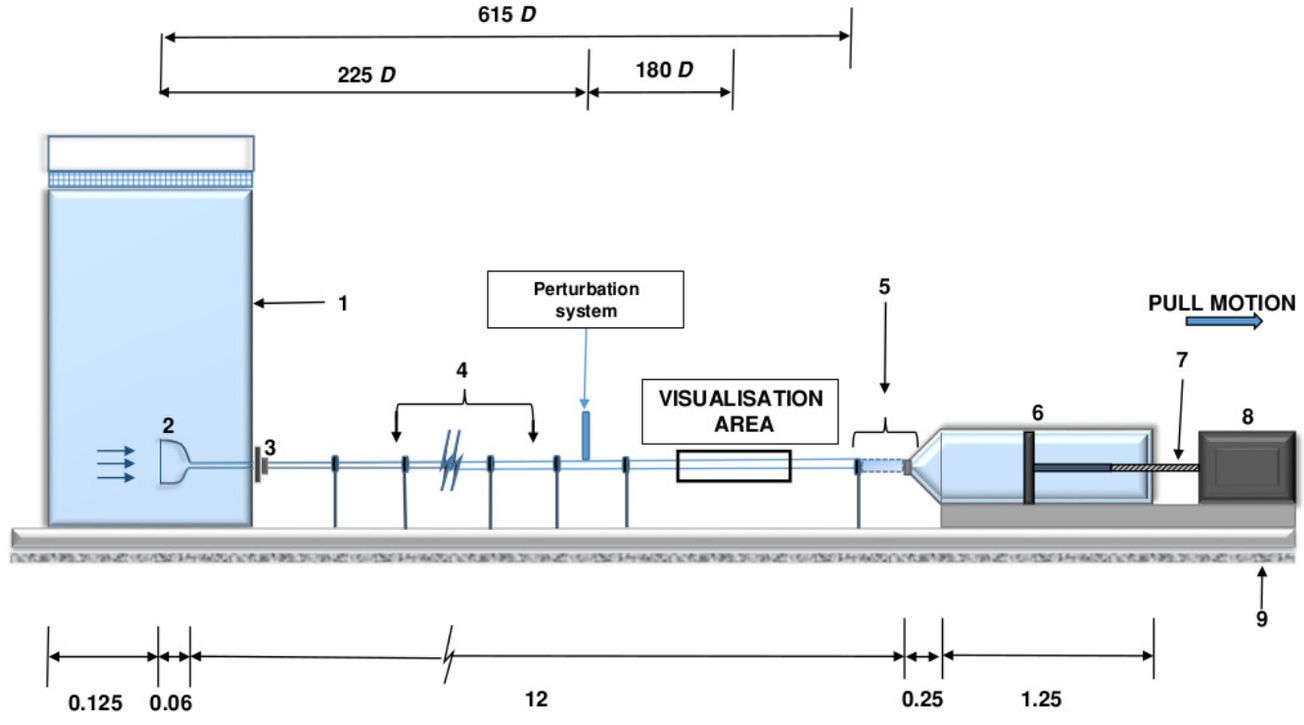

FIG. 1: A schematic diagram (front view) of the rig. (1) Reservoir, (2) Bell-mouth shaped inlet, (3) Flange, (4) Pipe sections held by unions on supports, (5) Flexible tube with a venturi, (6) Piston-Cylinder arrangement, (7) Lead screw, (8) Motor, (9) Adjustable Aluminium profile resting on concrete floor. The distance where the flow is perturbed, and the position of the visualisation area are marked in pipe diameters D. All dimensions are in meters. Drawing not to scale.

Eulerian velocities are obtained by PIV while Lagrangian velocities are obtained by PTV. For the measurement technique, a continuous wave (CW) LASER (OdicForce, 1 W) is used to generate a thin LASER light sheet (Thickness= 1 mm) with combination of a concave, a convex, and a cylindrical lens). Both phases are illuminated in a longitudinal plane, as shown in Fig.2. Successive images of the longitudinal plane are recorded by a camera (Photron Mini AX100) that can operate at 4000 Hz at a full resolution of $1,024 \times 1,024$ pixel, coupled with that of a macro lens (Tokina) with a shallow depth of field ($f-$number: 4). The measurement is conducted $180D$ downstream from the point where the perturbation is triggered. Some of the salient parameters of the PIV system are listed in Table III.

For an accurate measurement, the distortion of the images due to the curved walls of the pipe (hidden regions, multiple images and spurious displacements [14] have to be be avoided). To mitigate this, the measurement pipe section is immersed in a rectangular tank of 0.2 m length, 0.040 m height and 0.060 m depth filled with the working fluid. The density of the fluid in the visualization box is accurately matched to that inside the pipe. This removes the most important source of refractive distortion, leaving only a small distortion at the interface between the fluid and the glass pipe (of respective indices 1.524 and 1.33).

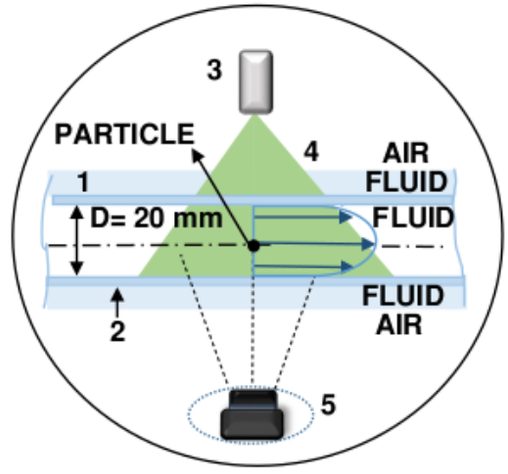

FIG. 2: LASER measurement plane: longitudinal. (1) Visualization box, (2) Pipe, (3) LASER, (4) LASER sheet, (5) Camera.

Light sheet	LASER type	CW
	Power	1 W
	Wavelength	532 nm
	Thickness	1 mm
Camera	Type	CMOS
	Resolution	1,024×1,024
	Sensor size	20.48 × 20.48 mm
	Pixel size	20 μm
	Discretisation	8 bit
	Frame rate	2000-4000 Hz
	Lens focal length	100 mm
Imaging	f-number	4
	Viewing area	0.027×0.027 m^2
	Primary Magnification (PMAG)	0.75X
PIV analysis	Interrogation area (IA)	32×32 px
	Overlap IA	75%
	Resolution (approx.)	0.84×0.84 mm^2
	Maximum tracer displacement	12 pixel
PTV		
	Average track length	13 frame
	Bin size	32×32 px

TABLE III: Some important parameters of the PIV system.

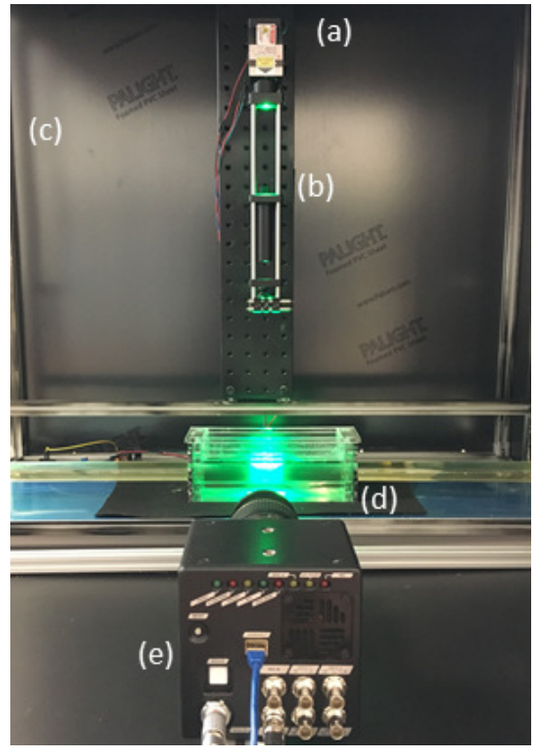

FIG. 3: Picture of the PIV setup. (a) LASER, (b) LASER sheet optics, (c) LASER box enclosure, (d) Visualization box, (e) Camera.

B. Calibration.

Accurate calibration is required to translate distances measured in pixel in the image into actual physical distances. For this, a calibration tool of dog-bone type is devised. The calibration tool is shown in Fig. 4 with its two grid sections annotated. It consists of a rectangular section of width, 19.8 mm and length, 50.1 mm with a lattice of 49× 20 dots of 1 mm size spaced evenly by 1 mm. The rectangular section is attached to a circular section in the middle. This circular section is of the same width as the diameter of the pipe. The rectangular section is used for calibration in longitudinal direction. This tool is inserted from the inlet using flexible plastic rods, and accurately aligned with the LASER sheet in the measurement section. This ensures that the systematic error is minimal. Images of the calibration grid are taken and then mapped onto a grid generated by `DaVis` software. A scale factor (1 mm= 27.83 pixel) is then calculated which is later used to rescale the images such that the images are in world coordinates. Note that the low level of distortion and the image processing technique we employ make it unnecessary to specifically correct distortion and reflections.

C. Image Processing

One of the key challenges at this step is to efficiently discriminate particles from tracers. In our experiment, the ratio of particle image diameter of tracer d_τ with that of solid particle, d_s is $d_s/d_\tau/ \approx 3.6$, satisfying the criterion for optimum detection [23]. The image diameters for tracer d_τ and the solid glass beads d_s are computed using [51]:

$$d_\tau = \sqrt{(Md_p)^2 + d_{diff}^2}. \quad (1)$$

M is the magnification factor[52] and d_{diff} is the diffraction-limited spot diameter given by:

$$d_{diff} = 2.44(1+M)f^{\#}\lambda, \quad (2)$$

here $f^{\#}$ is the f-number of the lens and λ the wavelength of the light. In Equation:1, the solid particle diameter d_p is replaced by tracer diameter d_t to compute the image diameter of the trace d_s.

Due to the differences in sizes and optical properties between the particles and the tracers [23], a phase discrimination method is first applied to detect and separate the two phases, using a tracking algorithm adapted from [42]. Following the separation, the PIV & PTV techniques can be applied. The image processing involves the following steps, as shown in the flowchart (Fig.5):

1. Removal of image distortions arising from background noise due to uneven illumination and specular reflections; the steady background images are removed by subtracting the global pixel mean of all images. This is

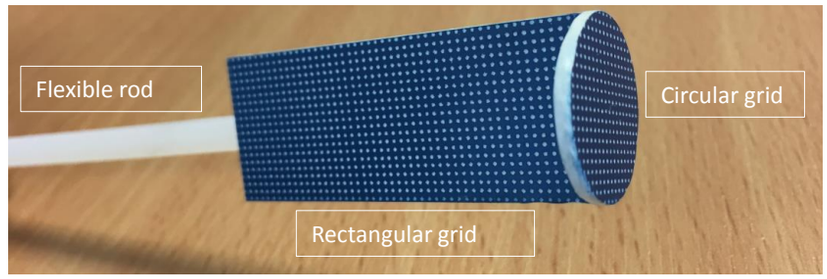

FIG. 4: Calibration tool is shown with the circular and rectangular grids attached to the rod.

carried out for both PIV & PTV;

2. Detection of bright particles (solid & tracers) by setting a brightness threshold *i.e.*, a local high intensity maximum in the restored images. Only the brightest "blobs" that differ from the background contrast by a prescribed brightness threshold are retained. This optimal threshold based on particles' brightness is chosen by plotting a gray-level histogram of the 21K images with the object average intensity I defined as brightness in x-axis, and number of pixels Npx in the y-axis. To illustrate the manner in which the parameter used to segregate the background from objects are chosen, a gray-level histogram from a two-phase experiment is shown in Fig. 6. A *bimodal* histogram is evident from the existence of two distinct regions of high values (corresponding to tracers and solid particles respectively) and background. The optimum threshold parameter to distinguish these two types of object is the point where approximate Gaussian fits for each of these regions intersect (in this case at a gray-level of 157 in the x-axis). Since the background dominates, the peaks in the particles distribution (tracers and solid) are small. Once the background is cut-off, the tracking algorithm is set to search for gray pixel areas greater than 1 pixel. The efficacy of this separation technique is illustrated in Fig.7, where a contour-plot of the size-brightness map of detected particle obtained from the search is plotted. Regions containing the tracer and the particles are represented by two distinct islands of higher particle count, standing well apart from each other. The size-brightness map [28] represents the total amount of signal of the particles where the quantity S represents the product of particle size, its brightness as maximum intensity I_{max} and number of particles detected N with the log of this product represented by the color scale. The images were not pre-processed with any filter and so appear to be slightly noisy.

   A clear separation appears between the tracer and particle intensities, illustrating the capacity of the tracking algorithm to successfully separate phases by choosing particles set by the parameters. The location of the centers of solid particles is determined by fitting two 1D Gaussian Estimator to the adjacent pixels, one for the horizontal position, the other for the vertical position. Since the intensity profile of particle image is not known, Gaussian profile is commonly assumed. This results in center estimation with a sub-pixel accuracy [41];

3. The solid particles detected in step (2) are accepted for tracking only if they undergo minimum displacement within the area of maximum allowable displacement threshold *i.e.*, a search window within which a detected particle is allowed to move between consecutive images. This generates an estimate for the measured particle position in x and y in each image. The tracks of detected particles are matched using a predictive three-frame best-estimate algorithm. This algorithm initially takes two images and uses nearest neighbor search to initiate linking of tracks. The tracks in subsequent frames are approximated using three image frames. Assuming least change in velocity in subsequent frames as the optimal solution, particles that remain within the specified search window are accepted as valid Lagrangian data. The Lagrangian data is then differentiated in time to generate time series of positions and velocities of tracked solid particles. The algorithm computes the time derivatives by convolution with a Gaussian smoothing and differentiating kernel using the method proposed by [53]. An optimum choice of the filter width, w and the fit width, T was made by varying the two parameters and observing the length of tracks, the number of particle detected, and the L2 norm error. w= 1 pixel and $T = 2.5w$ pixel was chosen after the parametric tests.

   This algorithm handles overlapping particles by ending tracks at point of overlap, and starting new tracks. This increases the data yield compared to an algorithm which cancels conflicting tracks. More algorithmic details of the tracking code can be found in [41].

4. Finally, the liquid phase is separated from the solid phase by dynamic masking. Logical masks using the x and y co-ordinates of the particles detected in step (3) in each frame are set to the background image pixel, thus leaving the images with tracers only. The particles are masked by circles of the same size as the particles. These circles are generated using a MATLAB function, and filled with pixels of the same grey level as the back-

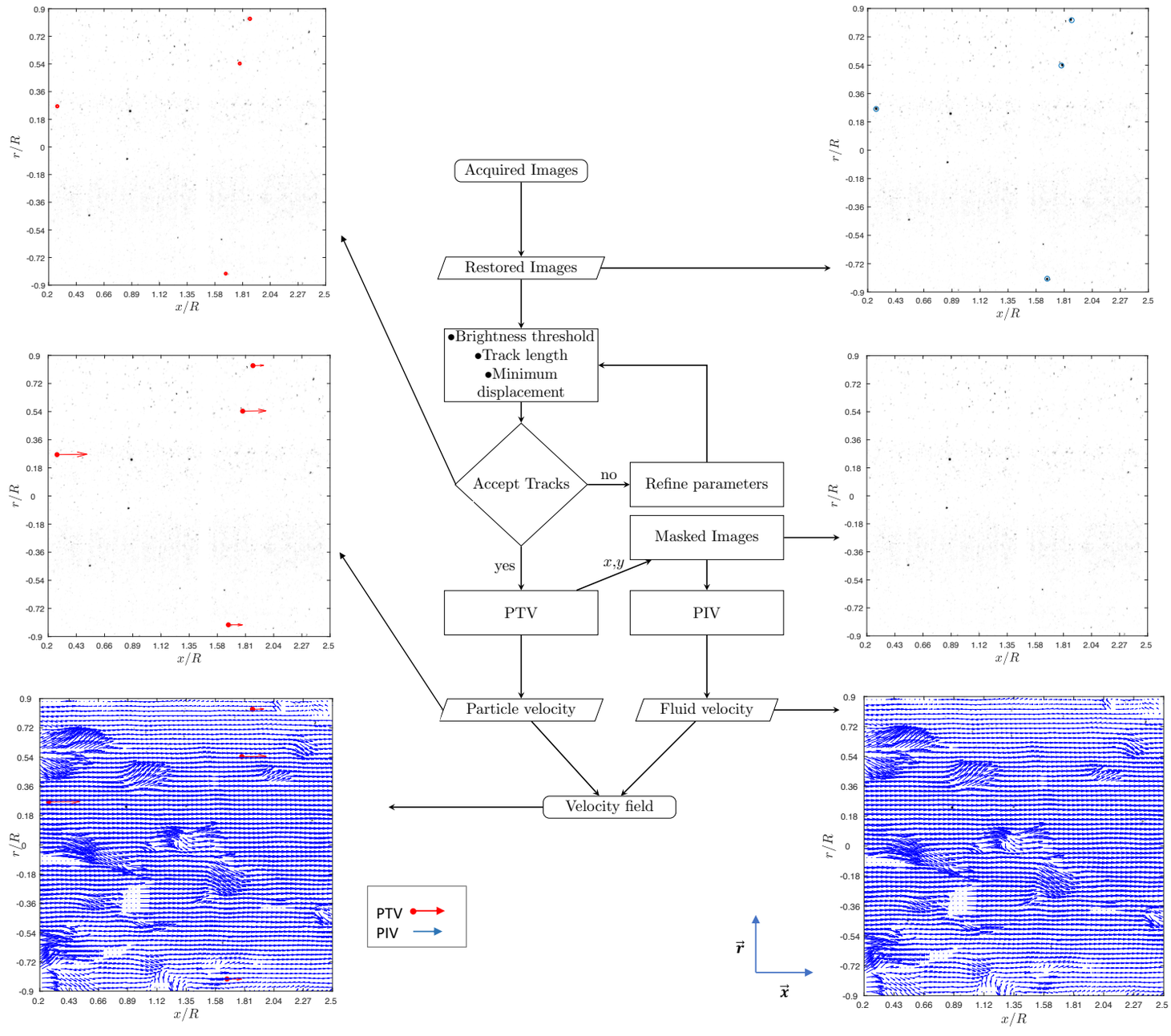

FIG. 5: Schematic representation of the procedure to measure both the Lagrangian velocity of particles and the Eulerian fluid velocities from the same set of an image. A typical snapshot of the flow image is shown with colors inverted for clarity (first 256 gray values only). Acquired raw images are restored to TIFF images on which the PTV algorithm is run after the background removal. Detected particles (shown in red) undergo PTV processing to obtain the Lagrangian vectors. Followed by masking where detected particles are removed, and the image containing only the fluid phase (tracers) undergo PIV processing to generate Eulerian velocity (shown in blue).

ground. In addition, the masked images are pretreated by a 3×3 median filter to remove any leftover traces of "coronas" of partially masked during pre-processing [22, 54]. Since the median filter tends to dim the image of particles, a sharpening filter is applied to images once they contain tracers only. Finally, the images are processed using standard PIV data analysis software (`DaVis` 10) to obtain the fluid velocity field. During the `DaVis` processing, the images are cleared of any specular reflections by background subtraction. This step is followed by PIV processing wherein the images are cross-correlated in 4 passes starting with 128×128 px

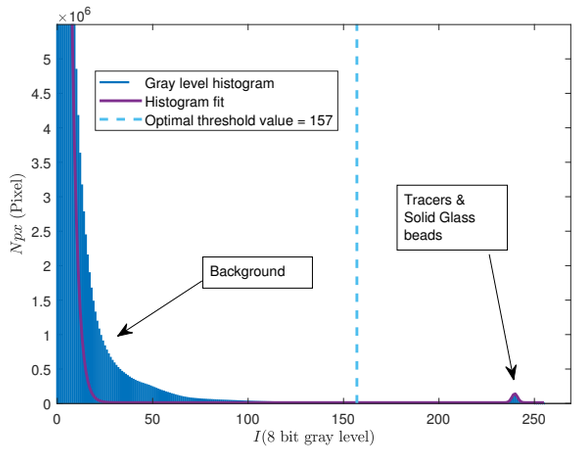

FIG. 6: Threshold for background separation based solely on particles' brightness. Gray-level histogram of the images with the object average intensity I defined as brightness, and Npx as the number of pixels. Two distinct histograms are seen, one for the solid particles and tracers, and another one for the background. The intersection of their respective Gaussian fits is indicated by the dashed line.

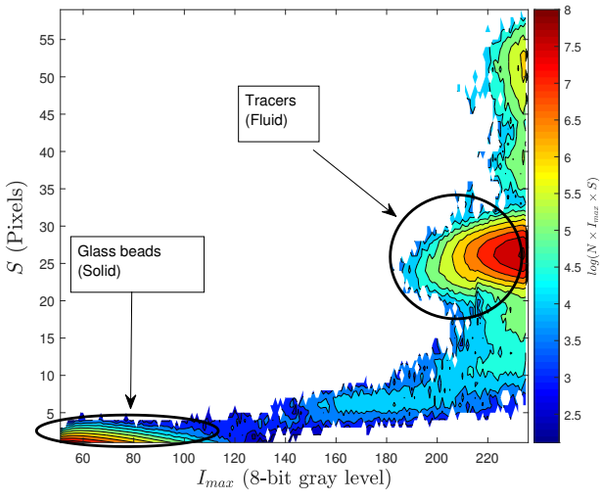

FIG. 7: Phase separation limit of regions of tracers and glass beads as illustrated by a size-brightness map where the quantity S represents the product of particle size, its brightness as maximum intensity I_{max} and number of particles detected N. The logarithm of this product is represented by the color scale.

interrogation window with 50% overlap, and ending in a final pass of a 32×32 px window with an overlap of 75%. The vectors with a dispersion of more than 2.5 standard deviation are iteratively removed and replaced. Using the methodology proposed by [55], `DaVis` computes the PIV uncertainty quantification of statistical quantities. To perform advanced statistics, the PIVMat Toolbox is used.

Additionally, an estimate of the "crosstalk" arising from the difficulty in estimating the phase separation was done using the method given by [56]. For our experimental conditions, it was found to be 0.0005% in the mean velocity and 0.038% in the RMS velocity, suggesting that this effect is negligible on fluid velocity for dilute concentration of solid particles such as in our experiments.

D. Experimental procedure

First, the fluid is mixed with tracers and glass beads, and stirred within the header tank. The fluid properties are then measured and recorded. The piston is first activated in alternative directions few times so as to homogeneously mix the suspension. Both particles and tracers remain in suspension for hours due to their extremely low settling velocity. There is an idling time of about 20 min before every experimental run to allow the fluid to become quiescent. This process is determined empirically, the idling time is longer after runs at higher Re.

For our measurements, the Reynolds number was in the range Re= 800-5060 and the solid particle concentration was set to C=10^{-5}. The LASER sheet was oriented in the longitudinal plane and the viewing area was approximately 0.027×0.027 m^2. The PIV images were taken during the pull motion of the piston. The image acquisition was triggered typically after 20 s of experimental run, and lasted for 5-10 s. The images are saved in a hard disk drive (HDD) in full depth, Raw image format and later exported as 8-bit TIFF (Tagged Image File Format) files for image processing. A typical acquisition generates a dataset of 39 GB, consisting of 21,841 images.

E. Validation of the processing technique on synthetic images

To estimate the PTV tracking error, synthetic images were used. `DaVis` was used to generate 4096 synthetic images of 1024 ×1042 px with randomly distributed particles of 2 px in size. The particles had a Gaussian intensity profile, and the seeding density was 0.001 particles per pixel (ppp). In addition, an additive Gaussian noise (25%) was added to the images, and the particles were given the same velocity as that of the background laminar flow (shift of 5-10 px) for which a reference velocity field based on a Poiseuille flow was generated. A sample synthetic image is shown in Fig. 8. While these conditions are reproduce the pipe configuration of the rig, the particle density and noise level are significantly higher than expected in actual experiment so as to obtain a robust assessment of the performance of the processing chain: The PTV tracking algorithm was run on these synthetic images. Taking the reference velocity field as the ideal case, the discrepancies in velocity field generated by the PTV was computed. The L2-norm of the error is plotted in Fig. 9, along with the reference streamwise velocity profile $U = \langle u_x(r) \rangle_t$, and the streamwise velocity profile using PTV algorithm respectively. The velocities are normalized by the centerline

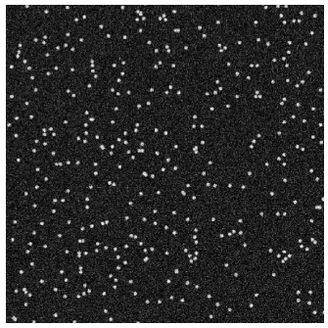

FIG. 8: A sample of cropped synthetic image (450×450 px) generated by `DaVis` is shown.

velocity, $U_0 = \langle u_x(r=0)\rangle_t$. The tracking algorithm follows

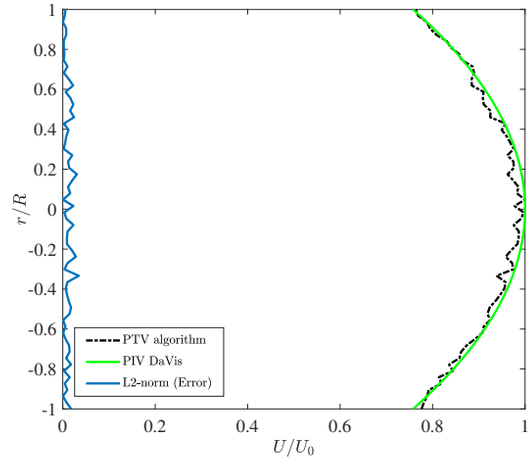

FIG. 9: Profiles of streamwise velocity obtained from synthetic images, $U = \langle u_x(r)\rangle_t$ scaled by U_0 against radial distance r scaled by pipe radius R, generated using the reference velocity field from `DaVis`, and by the PTV algorithm respectively. The L2 norm of the error incurred on the particle tracking is shown as well.

the reference velocity profile with a maximum error of 0.34 pixel/frame. The slight non-smoothness of the PTV profile is characteristic of Lagrangian data when they are averaged over smaller bins. This is typically improved by averaging over wider bins, or by gathering more data points. In real experiments, not only are density and noise level more favorable but the PTV algorithm is run on 21k images; suggesting that the error is further minimized, and definitely below the return level by this test.

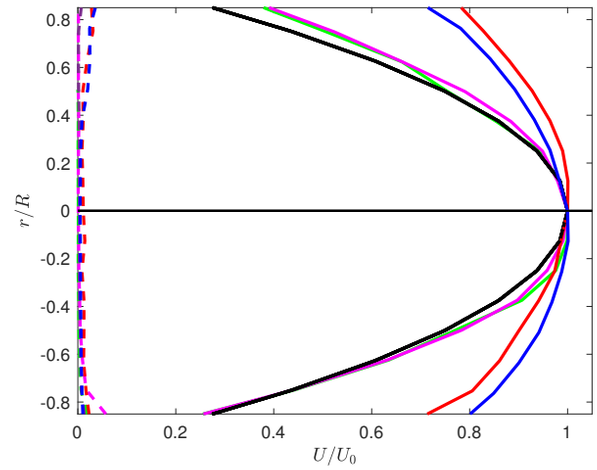

FIG. 10: The time-averaged streamwise velocity $U = \langle u_x(r)\rangle_t$ profile (scaled by centerline velocity $U_0 = \langle u_x(r=0)\rangle_t$) against radial distance r (scaled by pipe radius R) is shown for Re= 1200 (magenta curve), 2500 (green curve), 3575 (blue curve), 5060 (red curve) with their corresponding RMS fluctuations. The theoretical Poiseuille flow (black curve) is plotted for reference. Note that velocities within a distance of 0.1 r/R from the walls cannot be accurately measured because of reflections of the LASER on the wall surface, and have been excluded.

IV. PROFILES OF FLUID AND PARTICLES VELOCITIES

A. Single phase flow

The pipe flow was first characterized by a single phase experiment with the heavy fluid seeded with tracers only and no perturbation applied. PIV measurements were performed in the longitudinal plane, for values of Reynolds spanning Re= 1200-5060, so as to cover both laminar and turbulent regimes. No perturbation was applied. The mean streamwise velocity measurement obtained is shown in Fig.10. For $Re \leq 2800$, the time-averaged streamwise component of the fluid velocity, $U = \langle u_x(r)\rangle_t$, shows a typical Hagen-Poiseuille parabolic flow profile, in good agreement with the expected laminar theoretical profile. The profiles with Re= 3575 and Re= 5060 show a flatter profile, closer to what is expected from a turbulent flow. Inspection of the time-dependent flow-field reveals that intermittent bursts of turbulence are present in this regime, as expected in the transitional regimes. A snapshot of velocity norm scaled by U_0 is shown in Fig. 11 (Multimedia view) for Re= 3575.

Using the perturbation system, signals qualitatively resembling puffs and slugs can be seen in the velocity-time trace as shown in Fig.12. Their signatures clearly show fronts with sharp drops in their centerline velocities which have also been observed in past experiments [11, 15, 16]. While slugs are turbulent zone delimited by a sharp upstream and a downstream front, the downstream end of a puff is not well localized. Puffs

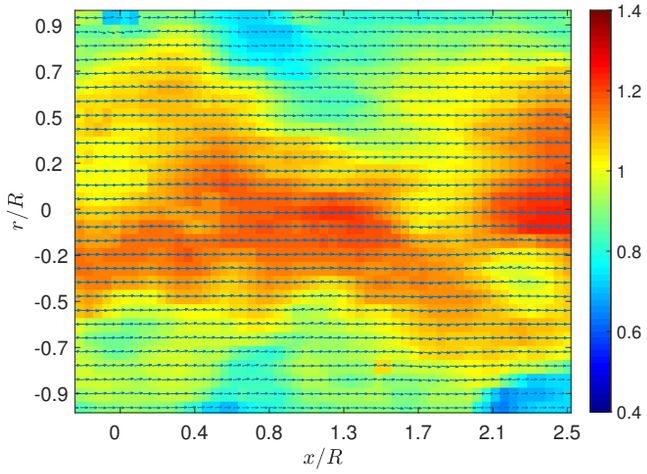

FIG. 11: A snapshot of single phase flow field with its velocity norm scaled by U_0 at Re= 3575 showing regions of turbulence (Multimedia view). Instantaneous velocities are shown in arrows.

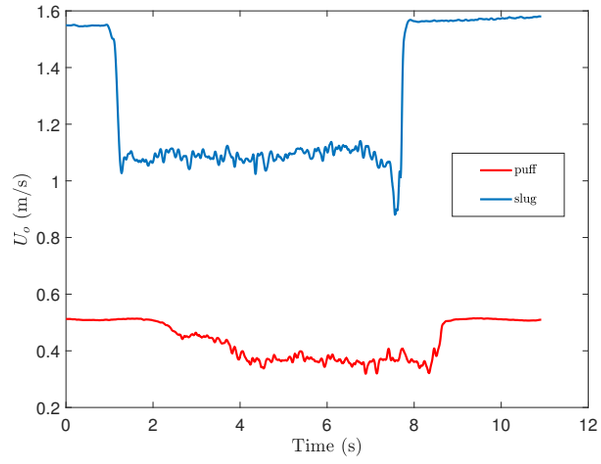

FIG. 12: Streamwise velocity time trace probed at the centerline $U_0 = \langle u_x(r=0)\rangle_t$ for single phase flow at $Re = 800$ (red curve) showing a puff, and $Re = 3400$ (blue curve) showing a slug.

are regions where patches of turbulence are present, and reflect an earlier stage of turbulence development than that of slugs, typically found at lower Reynolds numbers than slugs. For an impulsive perturbation jet of 0.75 ml with an injection time duration of 43 ms, a slug (blue) was seen at $Re = 3400$, and a puff (red) was observed at $Re = 800$. To obtain this, raw velocity data was smoothed by a Gaussian window (window length= 0.1% of the total frame number) chosen empirically. Following that, the time-dependent streamwise velocity at the centerline of the pipe is extracted. Since the measurements are done at one location, it is hard to conclusively categorize the flow structures, and infer if the appearance of puff and slug would lead to sustained turbulence eventually. However, their presence can be directly measured.

B. Two-phase flow

Next, we investigated a two-phase flow at low concentration C= 10^{-5}, St= 0.01-0.001 for a range of Reynolds numbers spanning Re= 800-3575. The average velocity profiles of both the fluid, and the solid phases are shown in Fig.13. Both are very close to the laminar Poiseuille profile. This result can be understood as follows: since at the current low particle concentration we consider, the influence of the solid particles on the flow is negligible, the fluid and the particles are only coupled one-way, with the solid particles acting as tracers [3, 10]. As the flow associated to the fluid phase is found laminar in this regime, the particle velocity profile also follows a Poiseuille profile. A snapshot of the velocity norm scaled by U_0 of the particulate flow at Re= 3575 illustrates this result in Fig. 14 (Multimedia view). Nevertheless, since in the single phase at the same Reynolds number, the flow is found turbulent, these results support earlier findings by [3] that the

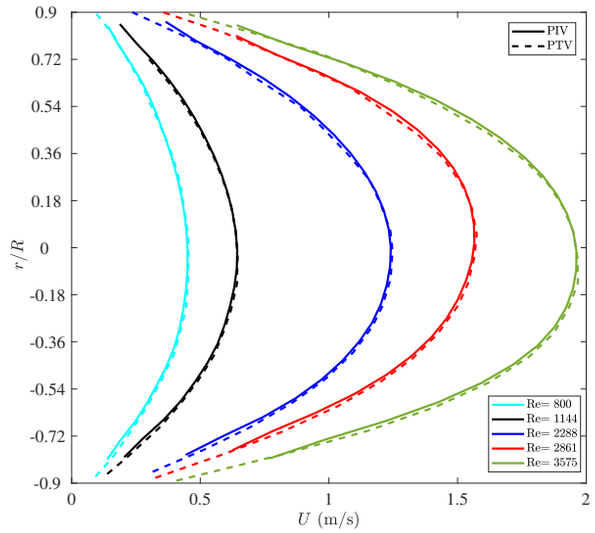

FIG. 13: Time-averaged streamwise velocity $U = \langle u_x(r)\rangle_t$ profiles against radial distance r (scaled by pipe radius R) for solid (dashed line) and fluid phases (solid line).

particles have a stabilizing effect.

The uncertainty in the time-averaged fluid velocity measurements, based on the discrepancy from a perfect cross-correlation (obtained from `DaVis`) was found to be within a range of 5-8% (mean velocities). The uncertainty in PTV measurement is computed using the RMS. Fig.15 shows the typical uncertainties in time-averaged streamwise velocity with their corresponding RMS fluctuations for PIV and PTV measurements. For reference, these are only shown for measurement at Re=2000 with the order of uncertainties remaining the same for measurements at other Reynolds numbers.

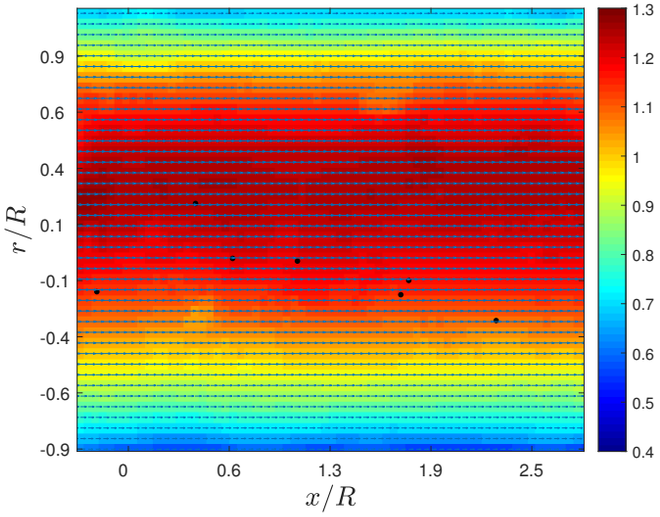

FIG. 14: A snapshot of the two-phase flow field with its velocity norm scaled by U_0 at Re= 3575 shows high centerline velocity typical of laminar flows. Instantaneous velocities are shown in arrows while the particles are shown as black dots (Multimedia view).

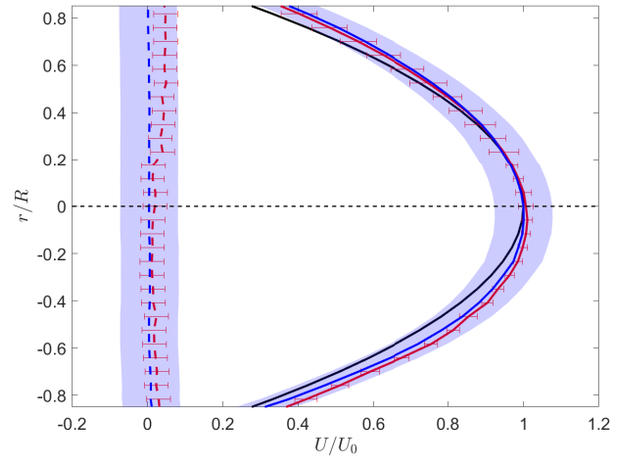

FIG. 15: Measurement uncertainties for PIV and PTV measurements at Re= 2000. The time-averaged streamwise velocity $U = \langle u_x(r)\rangle_t$ profile (scaled by centerline velocity U_0) against radial distance r (scaled by pipe radius R). Shaded area shows uncertainty for PIV, whereas the error bars are for PTV. Theoretical Poiseuille flow (black curve) and the pipe centerline (dotted black line) are shown as well.

As discussed in IV A, puffs and slugs can be triggered by injecting impulsive jets. They are clearly separated from regions of laminar flow by upstream front crossing the entire section of the pipe. In the case of slugs, a downstream front exists, whereas the tail end of puffs are less defined. However, tracing them using Lagrangian velocities of the particles is more complex than with the Eulerian velocity of the fluid phase. While centerline velocity in Eulerian velocity field is extracted

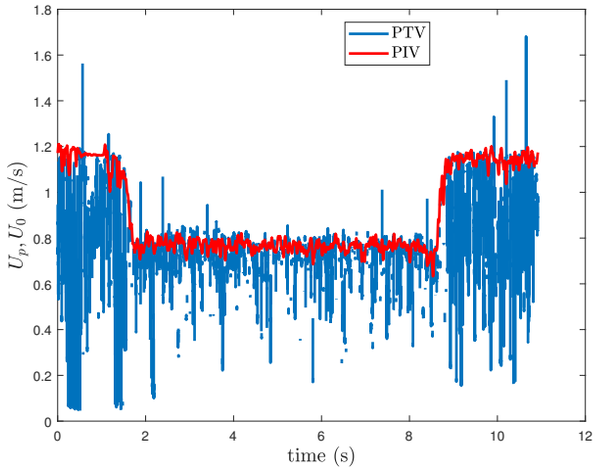

FIG. 16: Streamwise velocity time trace for a two phase flow at $Re = 2500$. Eulerian fluid velocity is shown in red (probed at centerline, $U_0 = \langle u_x(r=0)\rangle_t$), whereas the Lagrangian particle velocity U_p averaged over entire pipe diameter is shown in blue.

by simply positioning a "probe", this is not possible in Lagrangian data due to sparseness of such data. Instead, the discrete velocity data are averaged over a window of a specified size positioned at the centerline of the pipe. All particles detected in this window account for the average streamwise velocity of the particles U_p. Figure 16 shows velocity time trace of a slug at Re= 2500 using Eulerian (red) and Lagrangian (blue) velocities. The time evolution of particle velocities is noisy because data are collected from a large averaging window spanning areas of low velocity near the wall and of high velocity near the centerline.

However, when overlapped with the time evolution of the fluid velocity (probed at the centerline U_0 such that $U_0 = \langle u_x(r=0)\rangle_t$), the fronts in the particle velocity trace can be clearly observed and match very closely in this example. This is again a consequence of the passive advection of the small particles by the fluid phase.

V. SUMMARY AND CONCLUSIONS

We have presented a unique pipe flow facility with a novel optical measurement system, built for the express purpose of studying the transition to turbulence in particulate pipe flows. To this end, we have presented the first-ever simultaneous Eulerian-Lagrangian fluid-particle velocity measurements for very dilute (C= 10^{-5}), particulate pipe flow undergoing transition to turbulence within a range of $Re \in [800-3575]$. In addition, we have also demonstrated how image separation techniques, and an existing PTV tracking algorithm can be adapted to form a novel combined 2D PIV/ PTV technique. The masking and phase discrimination method we implemented is capable of successfully separating the phases. Moreover, the PTV algorithm performs well with negligible

tracking error. The experimental facility was shown to retain an undisturbed Poiseuille flow for *Re* up to 2500 for the single phase flow. On the other hand, the PIV/ PTV measurement system effectively captures known particle dynamics at low C, and is adept at characterizing transition by successfully tracing transitional flow patterns in both solid and liquid phases. These observations provide a validation of the experimental facility and the measurement system respectively for the future characterization of transitional particulate pipe flows. An early result is that even at low concentrations, small particles advected as tracers can prevent the transition to turbulence at a Reynolds number of 3575 where a transition would be observed in single phase.

The present technique nevertheless has certain limitations: it does not work with high particle concentrations when particles obscure each other and the linking of PTV tracks become erroneous (particle concentration of the order of 10^{-2}). Additionally, trajectories linking is possible only when single time step displacements of particles are reasonably small. This can be well mitigated by means of a high-speed camera. Similarly, for the PIV, images with more masked regions will render false velocity correlations. In principle, in planar PIV measurements these challenges can only be addressed to a certain extent by careful refractive index matching, or by adopting combinations of other existing algorithms [32, 38, 39]. For higher concentration measurements, 3D PIV/PTV or advanced techniques such as positron emission particle tracking have to be employed. However, our research does not aim to look at the effects of higher particle concentration. Given the various design and measurement challenges, this is the only measurement system that can successfully reconcile all of these constraints. To conclude, the present experimental facility with its unique measurement system is well suited to address the question of how a dilute-to-moderate concentration of particles affects the transition in pipe flows. Future evolution of our setup could also target particulate pipe flows in fully turbulent regimes, and boundary layer regimes. These would, however, require a challenging downscaling of particulate size and extending the dual PIV-PTV technique presented here to dual micro-PIV-PTV, as well as a greater control of near-wall reflections.

ACKNOWLEDGMENTS

AP is supported by a Wolfson Research Merit Award from the Royal Society (grant WM140032)). CCTP is partly supported by EPSRC grant No. EP/P021352/1. We thank the Environmental Complexity Lab, Stanford University for making the Particle Tracking code freely available online. We would also like to thank Aymeric Allemand from École normale supérieure de Lyon (ENS Lyon) who participated in some of these experiments.

DATA AVAILABILITY

Raw data were generated at the Pipe flow facility in the Fluid and Complex Systems Centre, Coventry University. Derived data supporting the findings of this study are available from the corresponding author upon reasonable request.

[1] M. Gad-el Hak, *Flow Control: Passive, Active, and Reactive Flow Management* (Cambridge University Press, Cambridge, 2006).
[2] C. Crowe, J. Schwarzkopf, M. Sommerfeld, and Y. Tsuji, *Multiphase Flows with Droplets and Particles* (Taylor & Francis, Abingdon-on-Thames, 1997).
[3] J.-P. Matas, J. F. Morris, and E. Guazzelli, Phys. Rev. Lett. **90**, 014501 (2003).
[4] Z. Yu, T. Wu, X. Shao, and J. Lin, Physics of Fluids **25**, 043305 (2013).
[5] G. Wang and D. H. Richter, Journal of Fluid Mechanics **868**, 538–559 (2019).
[6] J. Klinkenberg, H. C. de Lange, and L. Brandt, Physics of Fluids **23**, 064110 (2011).
[7] J. Klinkenberg, G. Sardina, H. C. de Lange, and L. Brandt, Phys. Rev. E **87**, 043011 (2013).
[8] A. Rouquier, A. Potherat, and C. C. T. Pringle, arXiv e-prints (2019), arXiv:1903.10389 [physics.flu-dyn].
[9] S. Boronin, Fluid Dynamics **47**, 351 (2012).
[10] A. Rouquier, A. Pothérat, and C. C. T. Pringle, Journal of Fluid Mechanics **870**, 247–265 (2019).
[11] A. G. Darbyshire and T. Mullin, Journal of Fluid Mechanics **289**, 83–114 (1995).
[12] J. Peixinho and T. Mullin, Journal of Fluid Mechanics **582**, 169 (2007).
[13] M. Nishi, B. Ünsal, F. Durst, and G. Biswas, Journal of Fluid Mechanics **614**, 425–446 (2008).
[14] B. Hof, C. W. H. van Doorne, J. Westerweel, F. T. M. Nieuwstadt, H. Faisst, B. Eckhardt, H. Wedin, R. R. Kerswell, and F. Waleffe, Science **305**, 1594 (2004).
[15] I. J. Wygnanski and F. H. Champagne, Journal of Fluid Mechanics **59**, 281–335 (1973).
[16] I. Wygnanski, M. Sokolov, and D. Friedman, Journal of Fluid Mechanics **69**, 283–304 (1975).
[17] T. Mullin, Annual Review of Fluid Mechanics **43**, 1 (2011).
[18] W. Hogendoorn and C. Poelma, Phys. Rev. Lett. **121**, 194501 (2018).
[19] N. Agrawal, G. H. Choueiri, and B. Hof, Phys. Rev. Lett. **122**, 114502 (2019).
[20] R. J. Adrian and J. Westerweel, *Particle image velocimetry* (Cambridge University Press, Cambridge, 2011).
[21] C. Poelma, J. Westerweel, and G. Ooms, Experiments in Fluids **40**, 347 (2006).
[22] C. Brucker, Lecture series-van Kareman Institute for fluid dynamics **1**, J1 (2000).
[23] K. T. Kiger and C. Pan, Journal of Fluids Engineering **122**, 811–818 (2000).
[24] M. L. Jakobsen, W. J. Easson, C. A. Greated, and D. H. Glass, Measurement Science and Technology **7**, 1270 (1996).
[25] K. T. Kiger and C.Pan, Journal of Turbulence **3**, N19 (2002).
[26] P. L. Knowles and K. T. Kiger, Experiments in Fluids **52**, 697 (2012).
[27] Y. Cheng, S. Pothos, and F. J. Diez, Experiments in Fluids **49**, 1375 (2010).

[28] D. A. Khalitov and E. K. Longmire, Experiments in Fluids **32**, 252 (2002).
[29] M. Elhimer, O. Praud, M. Marchal, S. Cazin, and R. Bazile, Journal of Visualization **20**, 289 (2017).
[30] N. Deen, J. Westerweel, and E. Delnoij, Chemical engineering and technology **25**, 97 (2002).
[31] J. Kolaas, D. Drazen, and A. Jensen, Journal of Dispersion Science and Technology **36**, 1473 (2015).
[32] S. B. Dalziel, Applied Scientific Research **49**, 217 (1992).
[33] S. Anders, D. Noto, M. Seilmayer, and S. Eckert, Experiments in Fluids **60**, 68 (2019).
[34] A. Masullo and R. Theunissen, Experiments in Fluids **58**, 70 (2017).
[35] S. Wiederseiner, N. Andreini, G. Epely-Chauvin, and C. Ancey, Experiments in Fluids **50**, 1183 (2011).
[36] S. Zade, P. Costa, W. Fornari, F. Lundell, and L. Brandt, Journal of Fluid Mechanics **857**, 748–783 (2018).
[37] N. Chenouard, I. Smal, F. de Chaumont, M. Maška, I. F. Sbalzarini, Y. Gong, J. Cardinale, C. Carthel, S. Coraluppi, M. Winter, A. R. Cohen, W. J. Godinez, K. Rohr, Y. Kalaidzidis, L. Liang, J. Duncan, H. Shen, Y. Xu, K. E. G. Magnusson, J. Jaldén, H. M. Blau, P. Paul-Gilloteaux, P. Paul-Gilloteaux, P. Roudot, C. Kervrann, F. Waharte, J.-Y. Tinevez, S. L. Shorte, J. Willemse, K. Celler, G. P. van Wezel, H.-W. Dan, Y.-S. Tsai, C. Ortiz de Solórzano, J.-C. Olivo-Marin, and E. Meijering, Nature methods **11**, 281—289 (2014).
[38] W. Brevis, Y. Niño, and G. H. Jirka, Experiments in Fluids **50**, 135 (2011).
[39] I. Sbalzarini and P. Koumoutsakos, Journal of Structural Biology **151**, 182 (2005).
[40] J. C. Crocker and D. G. Grier, Journal of Colloid and Interface Science **179**, 298 (1996).
[41] N. T. Ouellette, H. Xu, and E. Bodenschatz, Experiments in Fluids **40**, 301 (2006).
[42] D. H. Kelley and N. T. Ouellette, American Journal of Physics **79**, 267 (2011).
[43] J. Oliveira, C. van der Geld, and J. Kuerten, International journal of multiphase flow **73**, 97 (2015).
[44] D. Schanz, S. Gesemann, and A. Schröder, Experiments in Fluids **57**, 70 (2016).
[45] M. Maxey, Annual Review of Fluid Mechanics **49**, 171 (2017).
[46] K. L. McCarthy and W. L. Kerr, Journal of Food Engineering **37**, 11 (1998).
[47] A. Gurung and C. Poelma, Experiments in Fluids **57**, 171 (2016).
[48] P. Fairhurst, M. Barigou, P. Fryer, J.-P. Pain, and D. Parker, International Journal of Multiphase Flow **27**, 1881 (2001).
[49] D. J. C. Dennis and F. M. Sogaro, Phys. Rev. Lett. **113**, 234501 (2014).
[50] B. Hof, A. Juel, and T. Mullin, Phys. Rev. Lett. **91**, 244502 (2003).
[51] M. Raffel, C. Willert, and J. Kompenhans, *Particle Image Velocimetry: A Practical Guide* (Springer-Verlag Berlin Heidelberg, Berlin, 2007).
[52] Ratio of horizontal sensor size of the camera to the field of view.
[53] N. Mordant, A. Crawford, and E. Bodenschatz, Physica D: Nonlinear Phenomena **193**, 245 (2004), anomalous distributions, nonlinear dynamics, and nonextensivity.
[54] J. Minier and J. Pozorski, *Particles in Wall-Bounded Turbulent Flows: Deposition, Re-Suspension and Agglomeration*, CISM International Centre for Mechanical Sciences (Springer International Publishing, New York, 2016).
[55] A. Sciacchitano and B. Wieneke, Measurement Science and Technology **27**, 084006 (2016).
[56] D. Li, X. Wang, and Q. Zhong, Journal of Hydraulic Research **48**, 250 (2010).

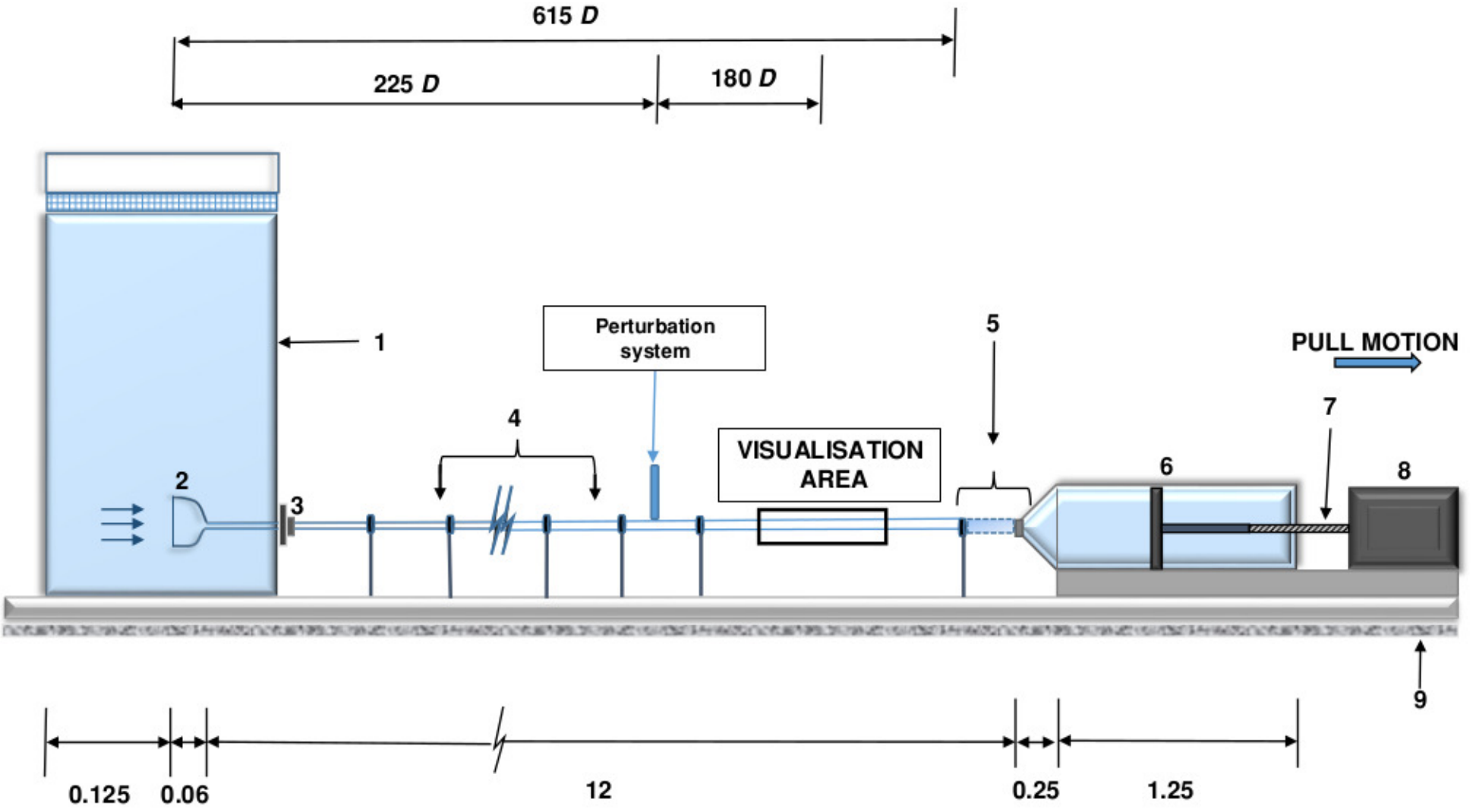
615 D
225 D
180 D
1
2
3
4
Perturbation system
5
VISUALISATION AREA
6
7
8
9
PULL MOTION
0.125
0.06
12
0.25
1.25

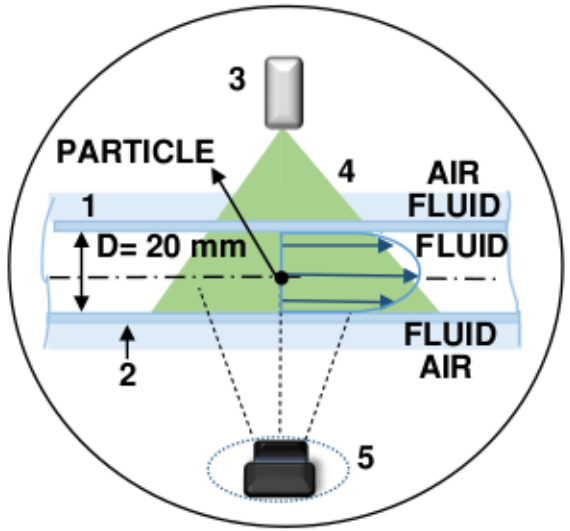
3
PARTICLE
4
AIR
1
FLUID
D= 20 mm
FLUID
FLUID
AIR
2
5

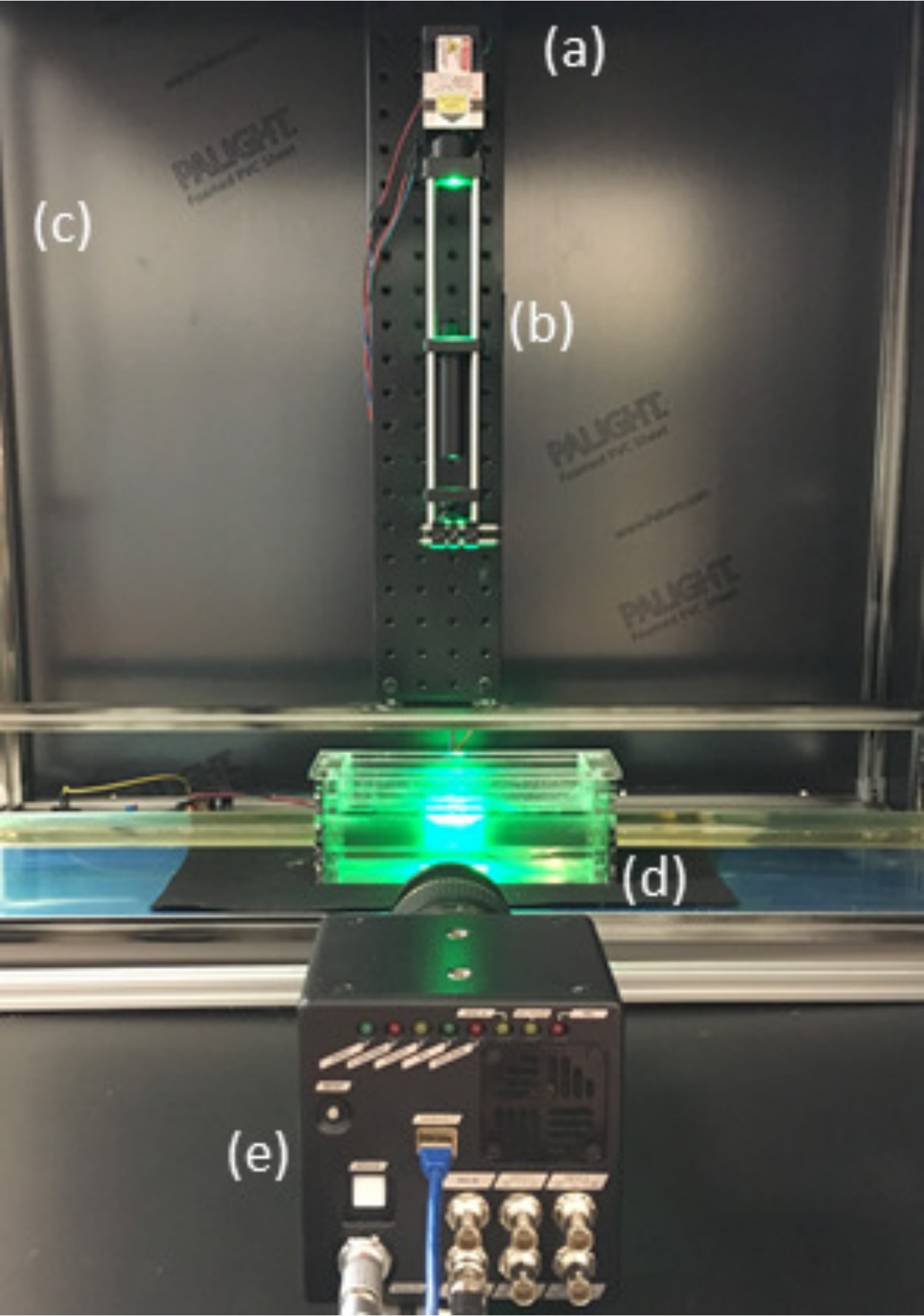
(a)
(b)
(c)
(d)
(e)

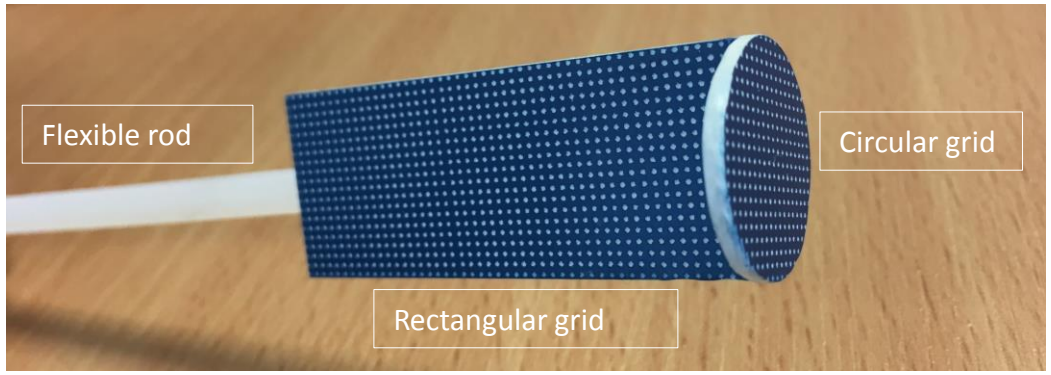
Flexible rod
Circular grid
Rectangular grid

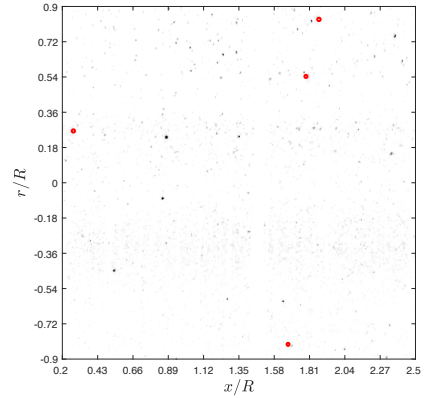

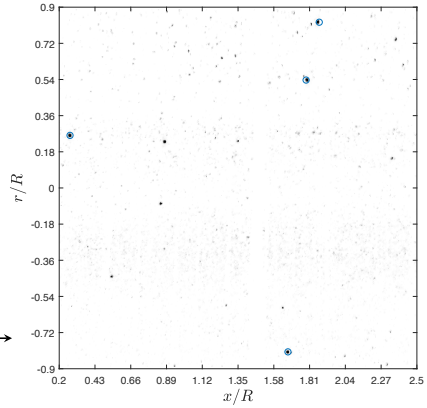

Acquired Images

Restored Images

•Brightness threshold
•Track length
•Minimum displacement

Accept Tracks

no

Refine parameters

Masked Images

yes

x,y

PTV

PIV

Particle velocity

Fluid velocity

Velocity field

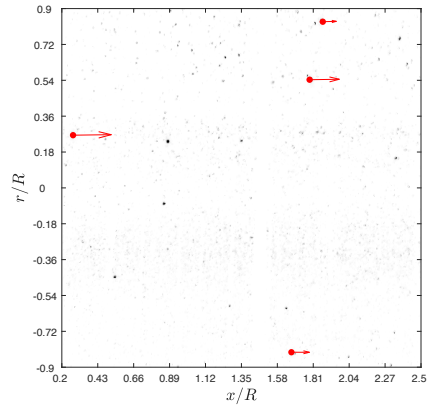

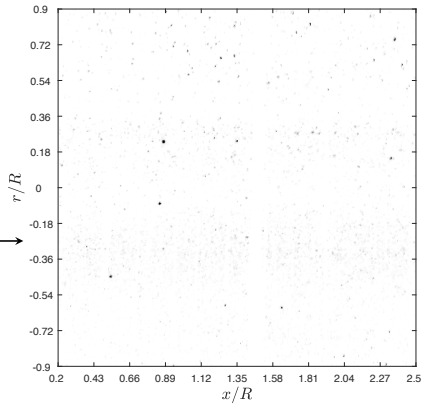

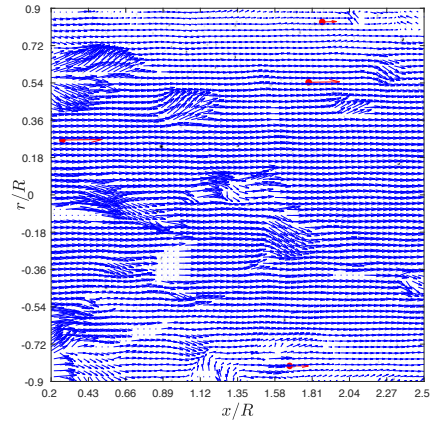

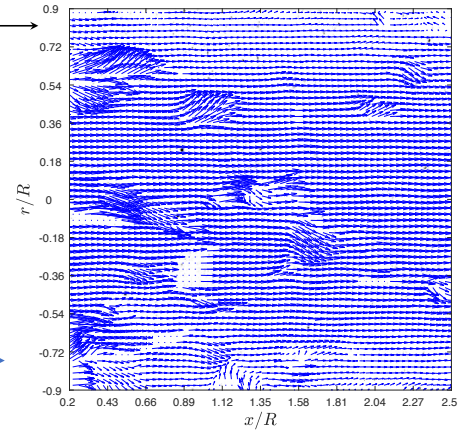

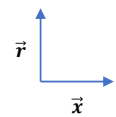

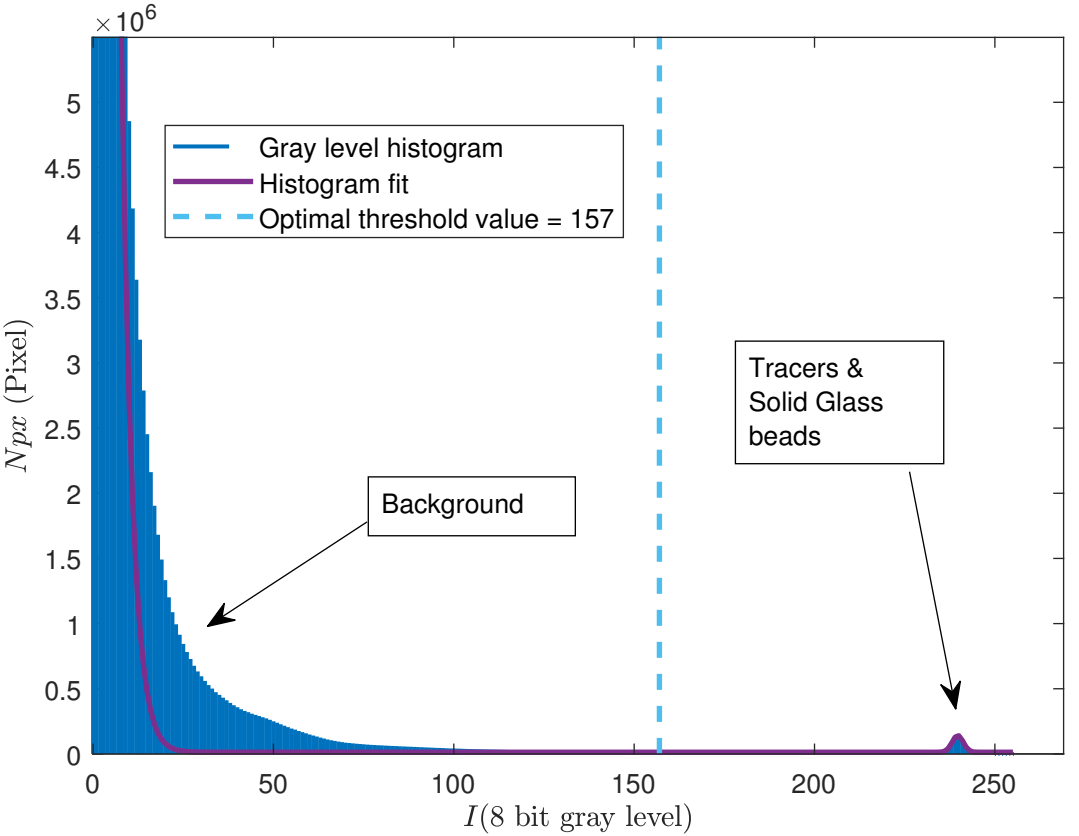
×10^6
5
4.5
4
3.5
3
2.5
2
1.5
1
0.5
0
Npx (Pixel)
Gray level histogram
Histogram fit
Optimal threshold value = 157
Background
Tracers &
Solid Glass
beads
0
50
100
150
200
250
I(8 bit gray level)

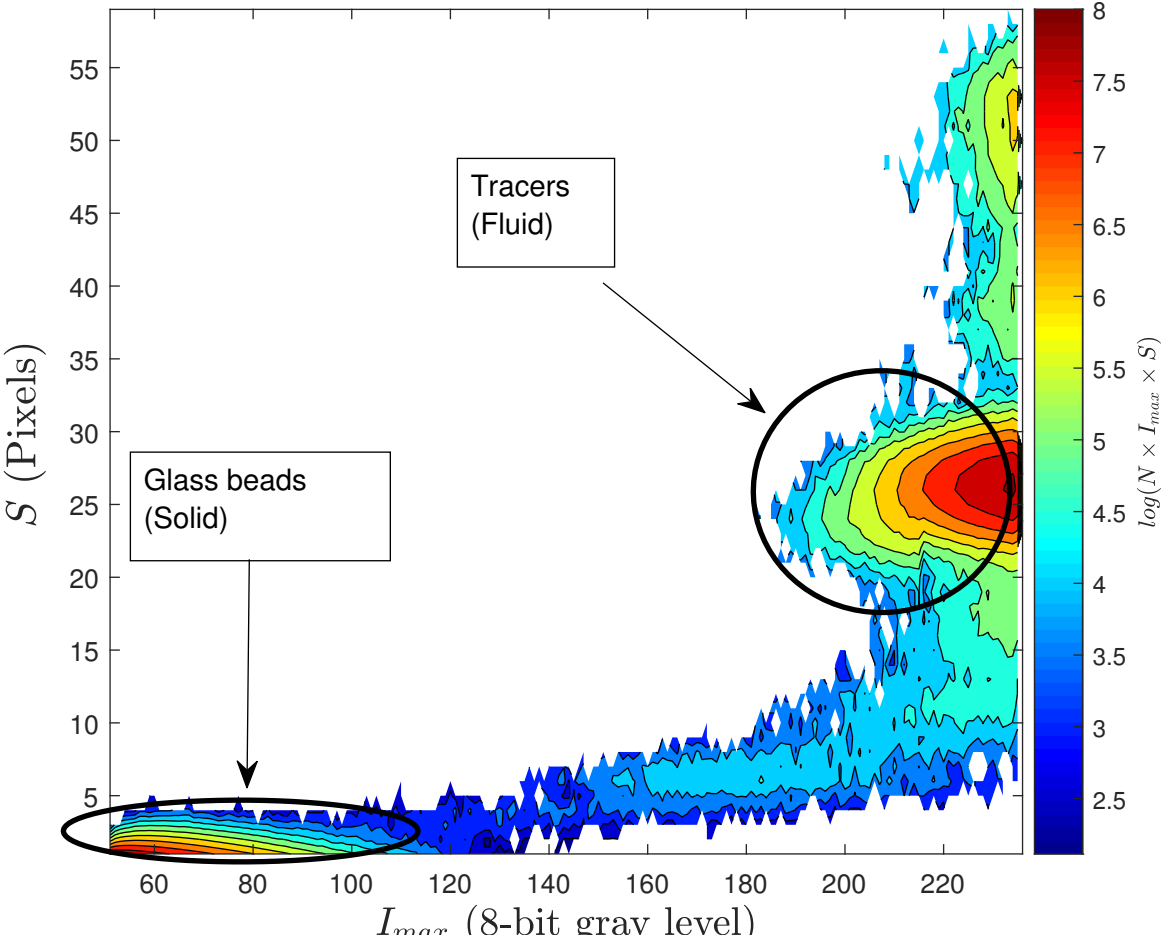
Tracers
(Fluid)
Glass beads
(Solid)
S (Pixels)
I_{max} (8-bit gray level)
$log(N \times I_{max} \times S)$
55
50
45
40
35
30
25
20
15
10
5
60
80
100
120
140
160
180
200
220
8
7.5
7
6.5
6
5.5
5
4.5
4
3.5
3
2.5

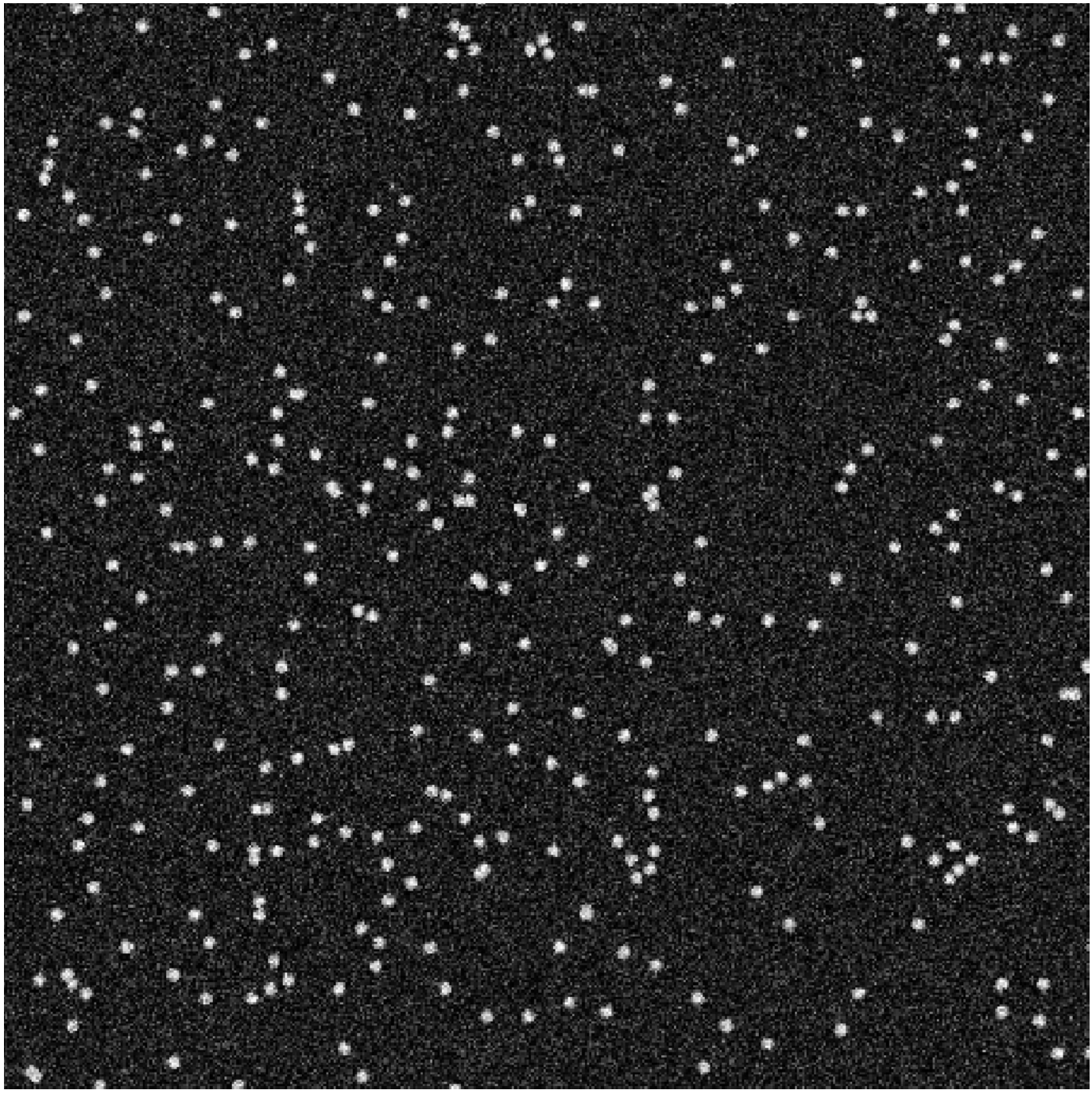

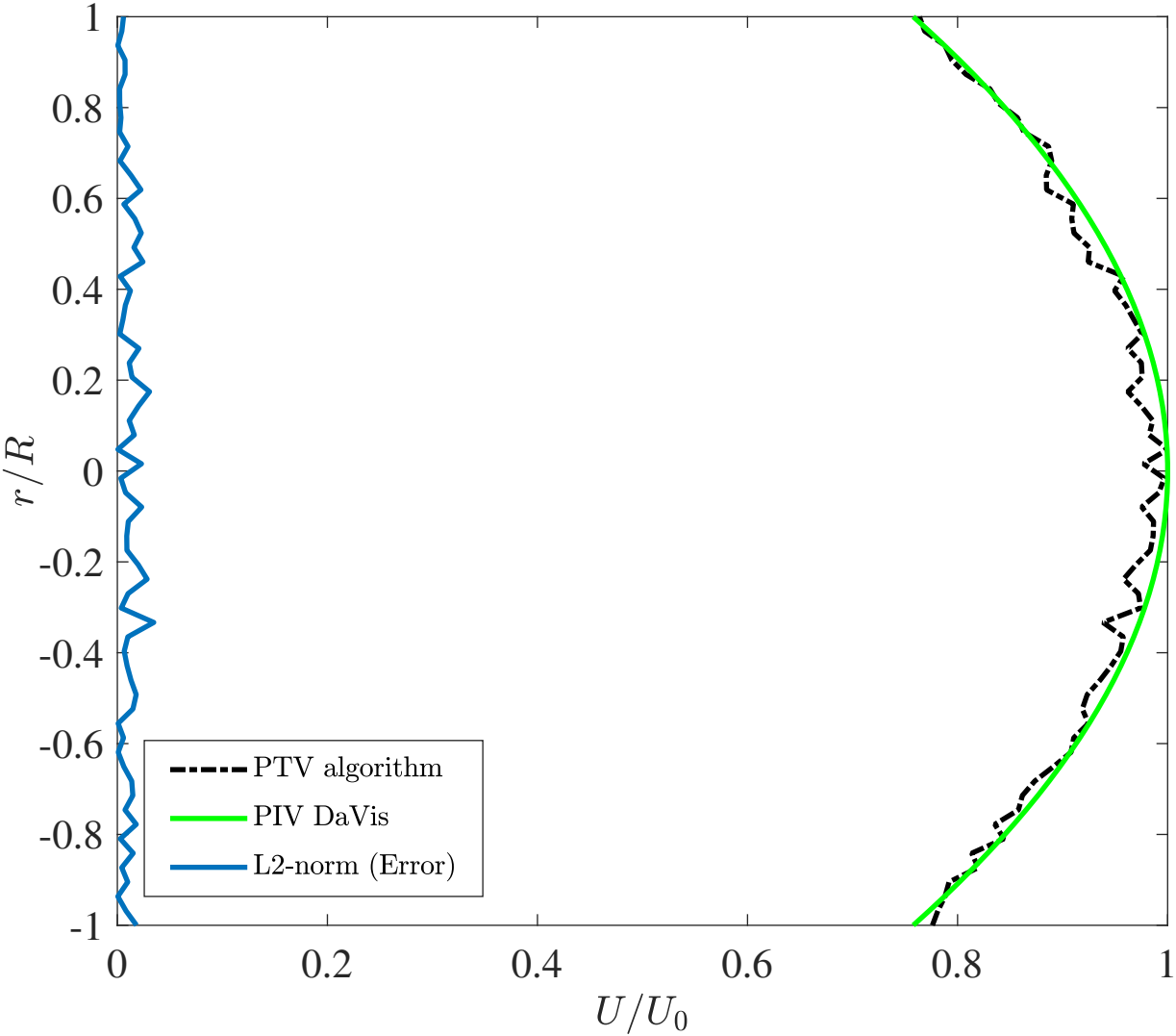
1
0.8
0.6
0.4
0.2
0
-0.2
-0.4
-0.6
-0.8
-1
r/R
0
0.2
0.4
0.6
0.8
1
U/U_0
PTV algorithm
PIV DaVis
L2-norm (Error)

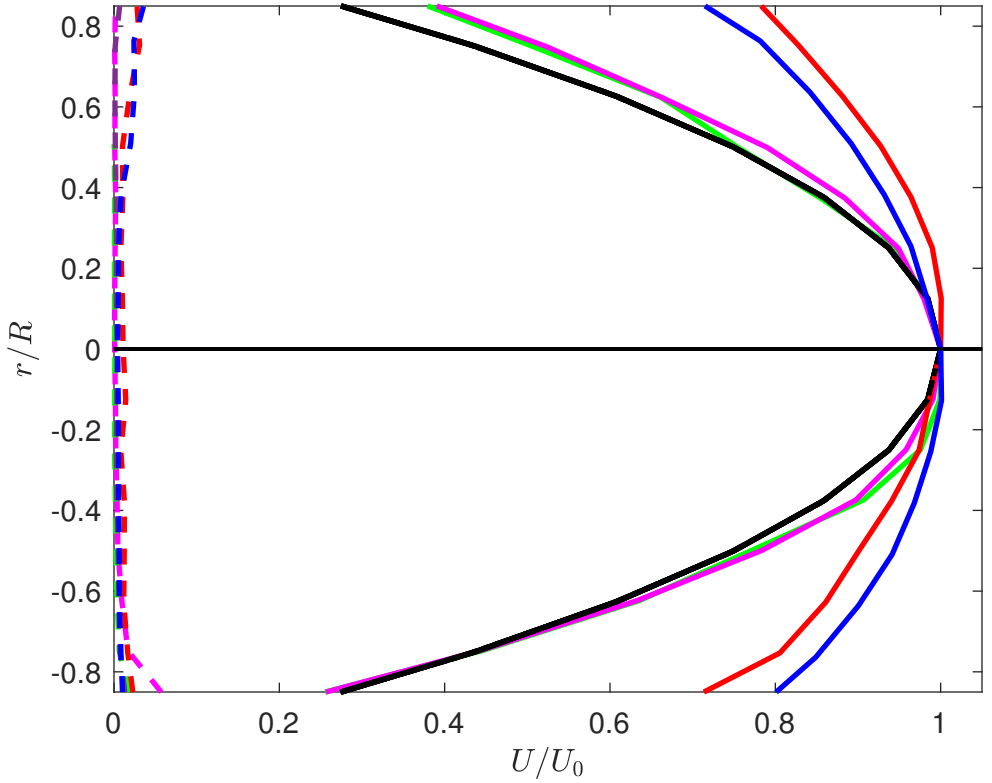
0.8
0.6
0.4
0.2
0
-0.2
-0.4
-0.6
-0.8
r/R
0
0.2
0.4
0.6
0.8
1
U/U_0

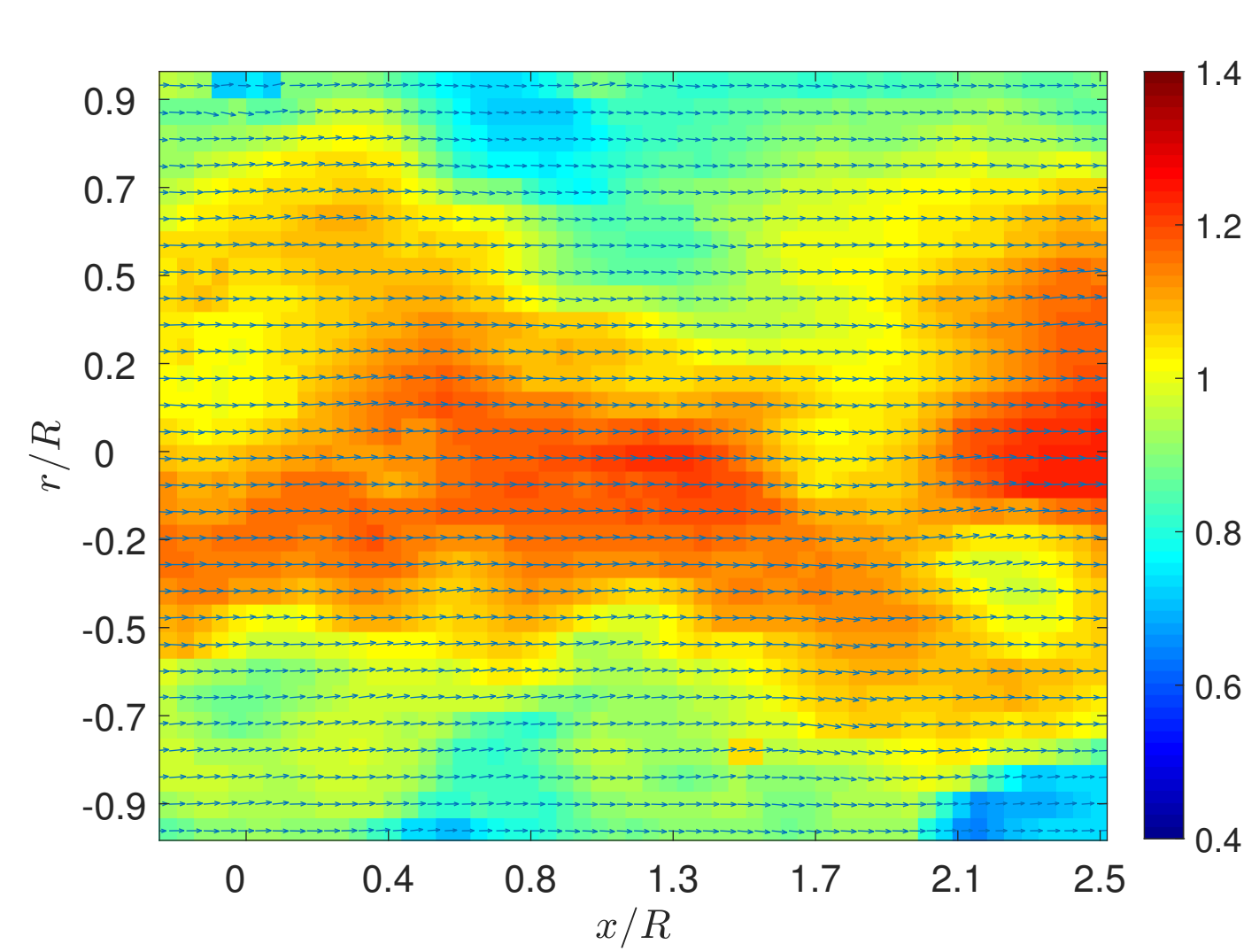
0.9
0.7
0.5
0.2
0
-0.2
-0.5
-0.7
-0.9
r/R
0
0.4
0.8
1.3
1.7
2.1
2.5
x/R
1.4
1.2
1
0.8
0.6
0.4

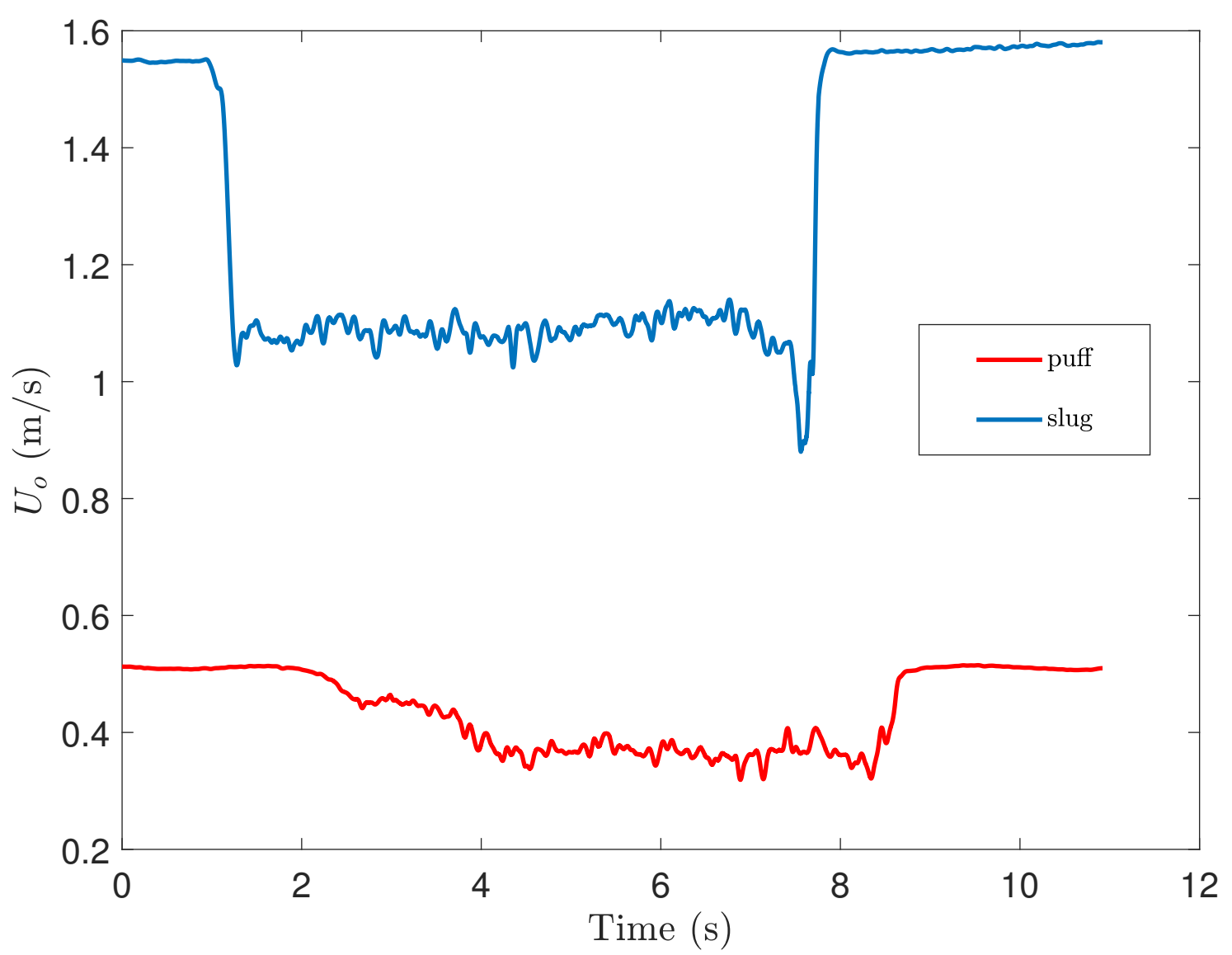
1.6
1.4
1.2
1
0.8
0.6
0.4
0.2
U_o (m/s)
0
2
4
6
8
10
12
Time (s)
puff
slug

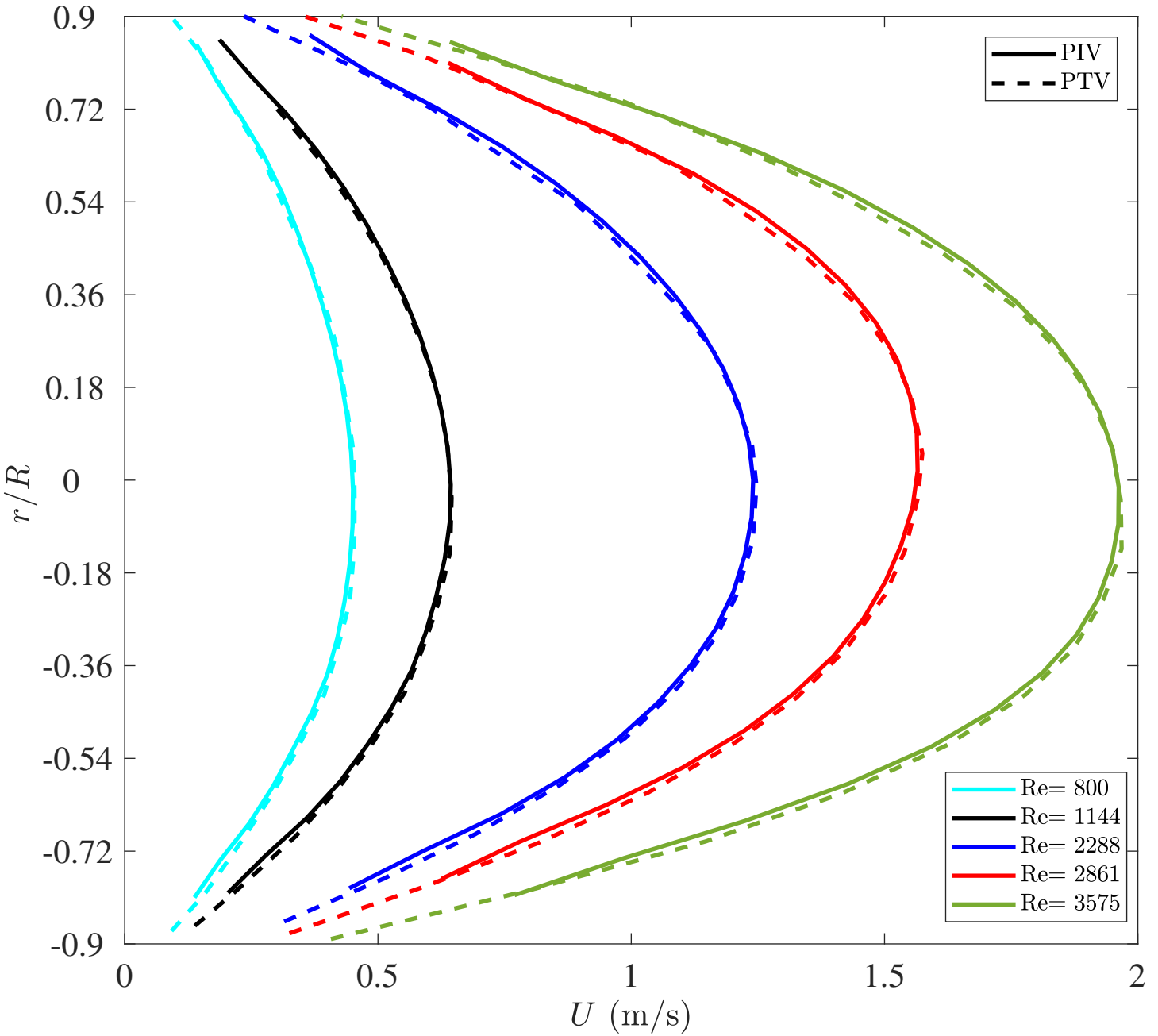
0.9
0.72
0.54
0.36
0.18
0
-0.18
-0.36
-0.54
-0.72
-0.9
r/R
0
0.5
1
1.5
2
U (m/s)
PIV
PTV
Re= 800
Re= 1144
Re= 2288
Re= 2861
Re= 3575

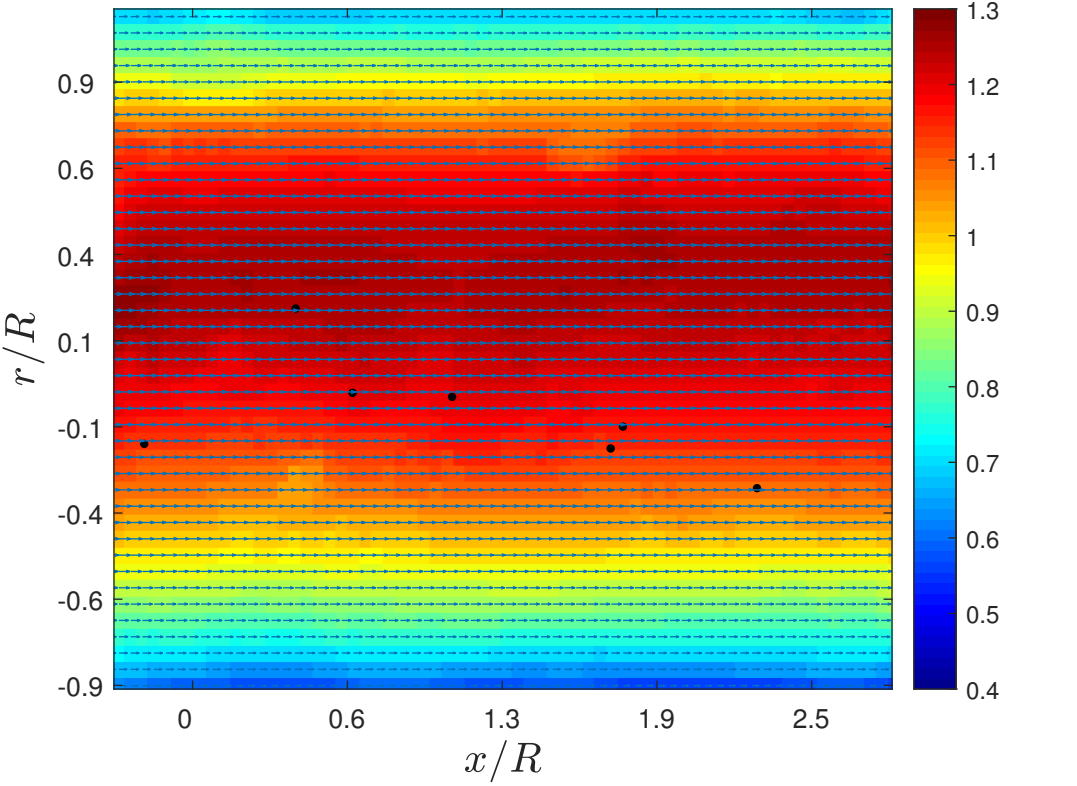
0.9
0.6
0.4
0.1
-0.1
-0.4
-0.6
-0.9
r/R
0
0.6
1.3
1.9
2.5
x/R
1.3
1.2
1.1
1
0.9
0.8
0.7
0.6
0.5
0.4

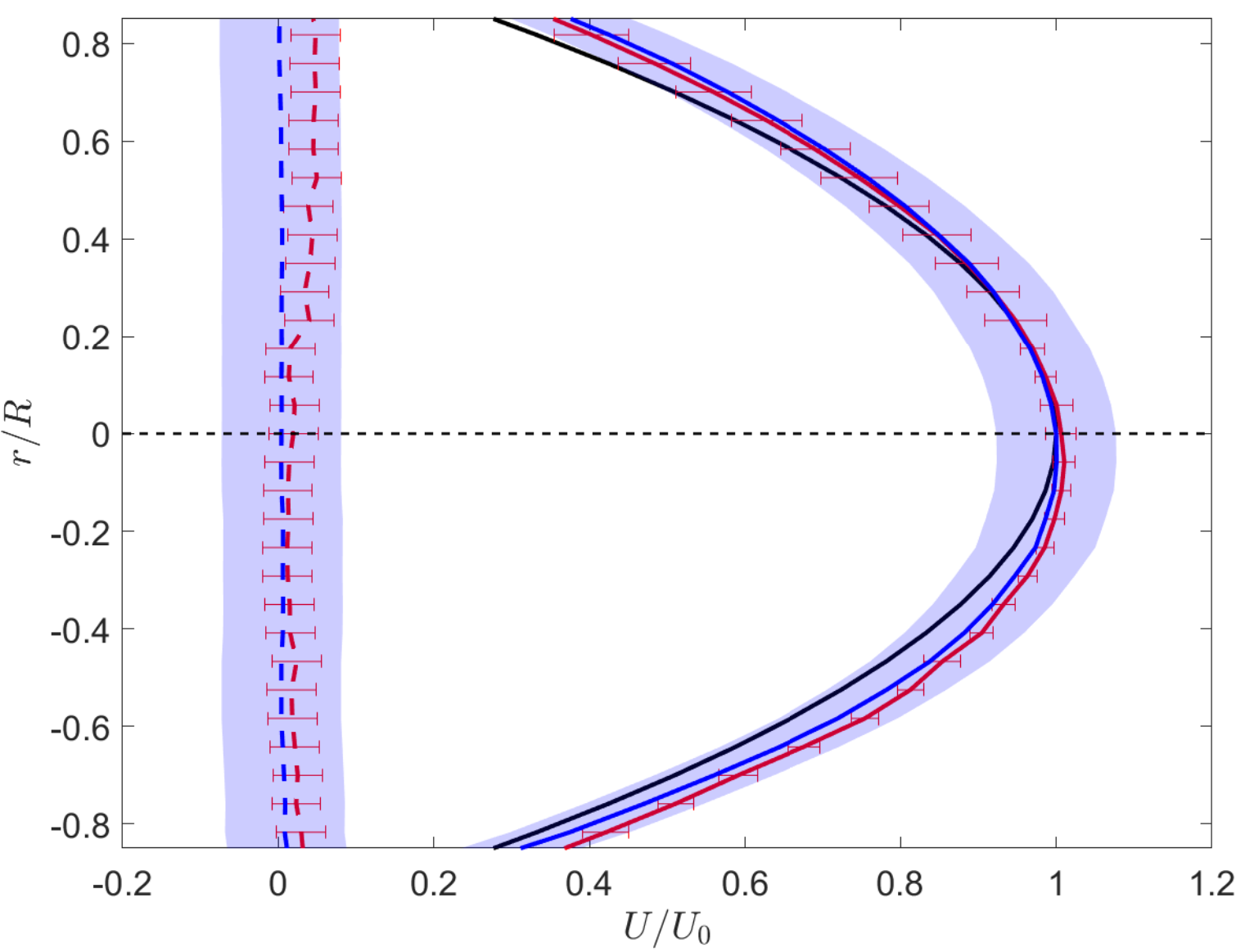
0.8
0.6
0.4
0.2
0
-0.2
-0.4
-0.6
-0.8
r/R
-0.2
0
0.2
0.4
0.6
0.8
1
1.2
U/U_0

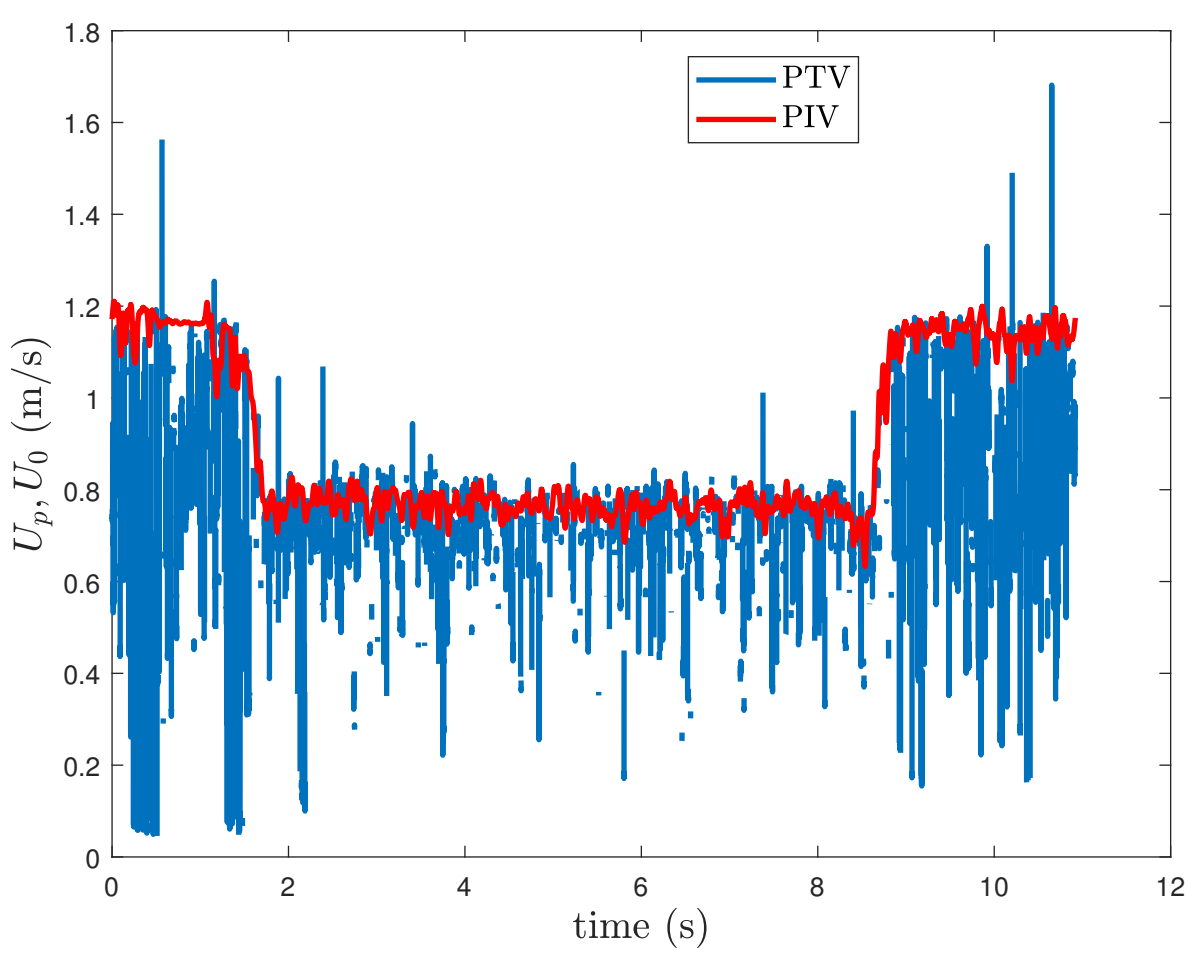
PTV
PIV
U_p, U_0 (m/s)
time (s)
0
0.2
0.4
0.6
0.8
1
1.2
1.4
1.6
1.8
0
2
4
6
8
10
12